ORNL/SPR-2024/3581
M3LW-24OR0403035

Light Water Reactor Sustainability Program

Assessment of Neutron-Induced Crack Volume on Aggregates of Varied Mineralogy and Estimation of Irradiation Damage Depth in the Concrete Biological Shield

Samantha Sabatino
Adam Brooks
Paula Bran Anleu
David Arregui Mena
Mark Rivers
Elena Tajuelo Rodriguez
Yann Le Pape

September 2024

U.S. Department of Energy
Office of Nuclear Energy

ORNL/SPR-2024/3581
M3LW-24OR0403035

Assessment of Neutron-Induced Crack Volume on Aggregates of Varied Mineralogy and Estimation of Irradiation Damage Depth in the Concrete Biological Shield

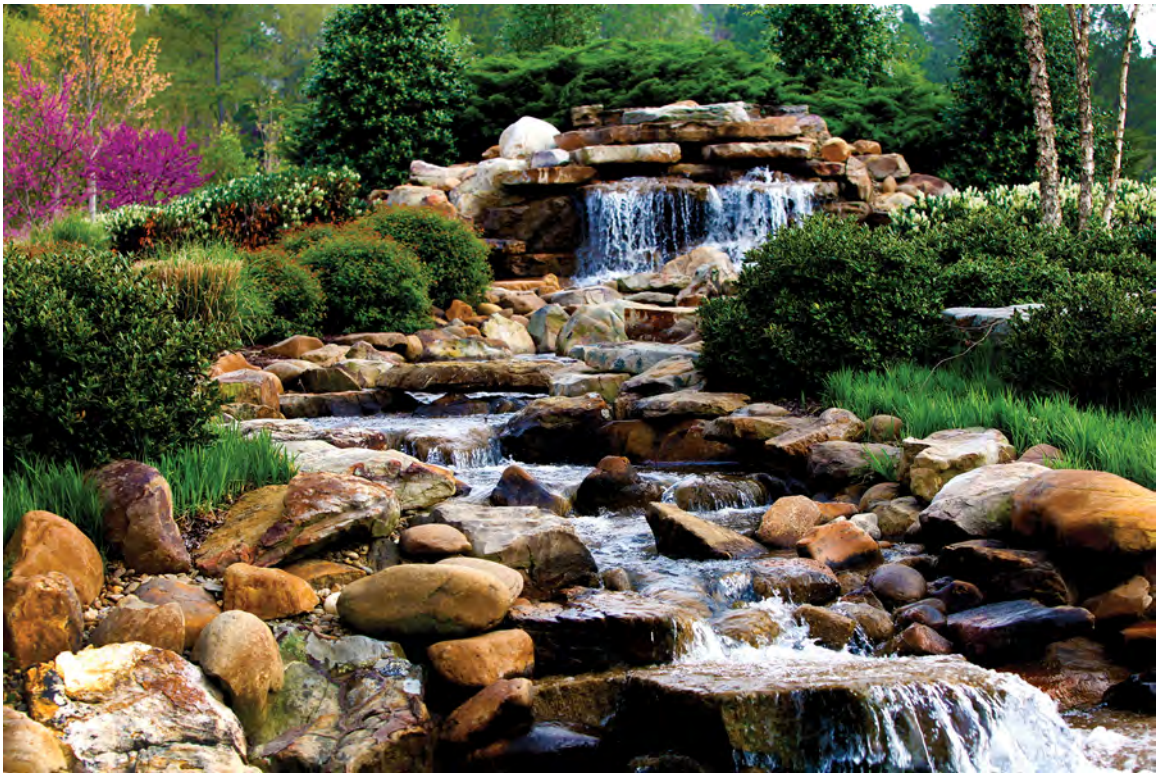

Samantha Sabatino[1]
Adam Brooks[1]
Paula Bran Anleu[1]
David Arregui Mena[1]
Mark Rivers[2]
Elena Tajuelo Rodriguez[1]
Yann Le Pape[1]

September 13, 2024

[1]Oak Ridge National Laboratory
[2]Advanced Photon Source, Argonne National Laboratory

OAK RIDGE National Laboratory

ORNL IS MANAGED BY UT–BATTELLE LLC FOR THE US DEPARTMENT OF ENERGY

ORNL/SPR-2024/3581
M3LW-24OR0403035

Nuclear Energy and Fuel Cycle Division

Material Science and Technology Division

ASSESSMENT OF NEUTRON-INDUCED CRACK VOLUME ON AGGREGATES OF VARIED MINERALOGY AND ESTIMATION OF IRRADIATION DAMAGE DEPTH IN THE CONCRETE BIOLOGICAL SHIELD

Samantha Sabatino[1]
Adam Brooks[1]
Paula Bran Anleu[1]
David Arregui Mena[1]
Mark Rivers[2]
Elena Tajuelo Rodriguez[1]
Yann Le Pape[1]

September 13, 2024

Prepared by
OAK RIDGE NATIONAL LABORATORY
Oak Ridge, TN 37831
managed by
UT-BATTELLE LLC
for the
US DEPARTMENT OF ENERGY
under contract DE-AC05-00OR22725

CONTENTS

LIST OF FIGURES

LIST OF TABLES

LIST OF ABBREVIATIONS

CBS	concrete biological shield
JCAMP	Japan Concrete Aging Management Program
LWR	light-water reactor
MD	molecular dynamics
NSSS	nuclear steam supply system
PDF	probability distribution function
PWR	pressurized water reactor
RIDD	radiation-induced damage depth
RIVE	radiation-induced volumetric expansion
ROI	region of interest
RPV	reactor pressure vessel
XRD	x-ray diffraction

EXECUTIVE SUMMARY

The primary function of the concrete biological shield (CBS) in light-water reactors (LWRs) is to protect equipment and personnel from neutron and gamma radiation escaping the reactor pressure vessel (RPV). Beyond this radioprotection role, the CBS in many pressurized water reactors (PWRs) also provides structural support to both the RPV and the nuclear steam supply system (NSSS). For the safe and viable long-term operation of LWRs, it is crucial to understand and characterize the effects of neutron and gamma radiation on concrete and its constituents, as well as to develop predictive tools to assess the performance of the CBS under both normal operating and accidental conditions.

The main degradation mechanism is the radiation-induced volumetric expansion (RIVE) of aggregate-forming minerals. The concrete in a LWR's biological shield is generally made of natural aggregate that constitutes about 70% of the concrete volume. Neutron irradiation causes the formation of defects (e.g., Frenkel pairs), voids, and the disordering of the crystalline structure of minerals. At its early stage, this phenomenon is called *amorphization* or *metamictization*. Such atomistic mechanisms lead to changes in the physical and chemical properties of minerals, including a change of density (expansive mechanism), the evolution of elastic properties toward isotropy, and acceleration in the dissolution rate of minerals in the presence of high-alkaline solutions, such as that of the cement paste porosity. Minerals' RIVE varies with the chemical composition and the ratio of covalent to ionic bonds. Highly covalent minerals such as quartz, which is a framework silicate, exhibit very large RIVE, up to nearly 18%. Other framework silicates, such as feldspars, may reach up to 8% in RIVE. The maximum RIVE decreases with less structured silicates such as pyroxene and olivine. Because silicates are abundant in the United States, their presence in a biological shield's concrete is very likely. Carbonates (i.e., calcite, dolomite) are much less susceptible to RIVE (maximum expansion estimated <0.3%). Metallic oxides, such as hematite and magnetite found in heavy aggregates, are sometimes used in boiling water reactors' CBSs. Their RIVE is on the order of a few percent.

Aggregates used for the construction of LWRs are extracted from quarries that encompass a range of geological formations, including magmatic, metamorphic, and sedimentary rocks. Regardless of the mechanisms involved in rock formation, aggregates are complex assemblages of various, and sometimes altered, minerals. The diversity of minerals within aggregates leads to mismatched RIVE between adjacent phases when they are subjected to neutron irradiation. This discrepancy results in the formation of both grain boundary and transgranular cracks, which deteriorate the mechanical properties of the aggregate. The extent of this deterioration depends on several factors, including the chemical composition of the aggregates (e.g., silica content); the rock formation mechanism, which influences grain size and boundary properties; and, ultimately, the presence of mineral defects.

Neutron-irradiated concrete is affected mainly by aggregate RIVE and cement paste shrinkage, which cause volumetric change and a degradation of mechanical properties, including Young's modulus as well as tensile and compressive strength at fluences $\gtrapprox 10^{19}$ n·cm^{-2} ($E > 0.1$ MeV). PWRs operating in the United States are expected to be subject to these fluence levels at 80 years of operation.

This report is centered on two different problems. The first part provides a probabilistic analysis of the damage depth in the biological shield, considering average mineralogical compositions of sedimentary rocks as aggregates. It was found that the penetration depth is highly correlated with the aggregate volume fraction. For typical aggregate volume fractions of 0.7, the average penetration depth was on the order of 8 cm. The probability of damage reaching beyond the rebar, which is located at 3 in. from the inner surface of the biological shield, is 0.58 for a fluence of 0.6 n·pm^{-2} ($E > 10$ keV). When damage reaches the steel rebar cage, this is indicative of the concrete cover spawling and the potential of the rebar being exposed to further damage.

The second part of the report describes a methodology to characterize volume fractions of neutron-induced cracks for aggregates of varied mineralogy, including some sedimentary rocks (i.e., sandstones), a tuff, and a limestone. Micro-XCT scans were analyzed using Dragonfly for crack volume segmentation. The results show that sandstones are the most affected rocks by irradiation, followed by the tuff and the limestone. This finding is in agreement with previous characterization of the same rocks and with the expected effects given their mineralogical origin. An accurate prediction of irradiation damage in concrete, especially the decrease in mechanical properties, relies on the characterization of the induced crack volume in the aggregate. The presented methodology is sample-preparation-free and is advantageous over other methods that have shown to have limitations, such as the analysis of scanning electron microscopy images.

ACKNOWLEDGMENTS

This research was sponsored by the US Department of Energy (DOE) Office of Nuclear Energy's Light Water Reactor Sustainability program Materials Research Pathway under contract DE-AC05-00OR22725 with UT-Battelle LLC/Oak Ridge National Laboratory (ORNL).

1. INTRODUCTION

The collision of fast neutrons ($E > 10$ keV) with the concrete constitutive materials of the concrete biological shield (CBS) causes point defects and atomic cascades. Aggregate-forming minerals are susceptible to irradiation damage. The physical mechanism of this deterioration is called *amorphization*: the pristine crystalline structure of the minerals is gradually distorted by deformation and rupture of their ionic and covalent bonds. Amorphization results in changes to physical and engineering properties: density (Primak 1958, 1976; Wong 1974; Denisov, Dubrovskii, and Solovyov 2012; Krivokoneva and Sidorenko 1971; Krivokoneva 1976), elastic properties (Mayer and Lecomte 1960; Krishnan et al. 2018), and dissolution susceptibility in the presence of high-pH solutions (Pignatelli et al. 2016; Hsiao et al. 2017; Hsiao et al. 2018; Hsiao et al. 2019). The main effect is called radiation-induced volumetric expansion (RIVE). Most minerals exhibit a gradual swelling with increasing fluence, generally in the form of sigmoidal curves (Bykov et al. 1981; Denisov, Dubrovskii, and Solovyov 2012; Le Pape, Alsaid, and Giorla 2018). However, there are exceptions to that rule: vitreous forms of quartz (e.g., chert, opal) exhibit shrinkage (Mayer and Lecomte 1960; Primak and Kampwirth 1968). The amplitude of RIVE varies greatly with the mineralogy, from $< 1\%$ in carbonates to $\sim 18\%$ in quartz (Primak 1958). A complete study on this topic can be found in (Denisov, Dubrovskii, and Solovyov 2012; Le Pape, Alsaid, and Giorla 2018). Expansion is anisotropic along the initial crystalline axis (Denisov, Dubrovskii, and Solovyov 2012). RIVE kinetics are affected by the irradiation temperature, causing thermal annealing (Bykov et al. 1981). Aggregates (i.e., rocks) are assemblages of minerals of varied chemical compositions and crystal orientation, and incompatible RIVEs cause the formation of voids and cracks, leading to a degradation in the engineering properties of these concrete aggregates and, subsequently, the concrete itself (Hilsdorf, Kropp, and Koch 1978; Seeberger and Hilsdorf 1982; Field, Remec, and Le Pape 2015). Whereas there is consensus about the existence of the fast-neutron damage mechanism in rock-forming minerals, the understanding and models developed to estimate rock-forming minerals' RIVE are based on post-irradiation examination of specimens irradiated in test reactors. These irradiation conditions exhibit fast neutron fluxes that are about 2 orders of magnitude higher than the typical flux in pressurized water reactors (PWRs). The same can be said about the gamma dose in some cases.

2. EFFECT OF MINERALOGY OF SEDIMENTARY TERRIGENEOUS ROCKS ON IRRADIATION DAMAGE

2.1 OBJECTIVES

This research builds upon previous work detailed in the LWRS milestone report titled "Effects of Aggregates' Mineralogy on Irradiation-Induced Damage in Concrete Biological Shields" (Le Pape, Sabatino, and Tajuelo Rodriguez 2023). The objective of this study is to evaluate how the mineralogy of silicate-bearing sedimentary aggregates—also known as *terrigenous sedimentary rocks*—affects the risk of irradiation-induced damage in concrete biological shields of pressurized water reactors (PWRs).

Carbonate-bearing sedimentary rocks (e.g., calcitic limestone, dolomite) are not considered herein because it was established that carbonate-bearing minerals are not prone to RIVE (Hilsdorf, Kropp, and Koch 1978; Denisov, Dubrovskii, and Solovyov 2012).

To associate the material and structural performance of irradiated concrete to the mineral composition of the concrete-forming aggregates, a multiscale approach combining previously developed empirical and analytical models at the mineral scale (Le Pape, Alsaid, and Giorla 2018), the aggregate scale (Le Pape, Sanahuja, and Alsaid 2020), the concrete scale (Le Pape, Field, and Remec 2015), and the structural scale (Le Pape 2015) was implemented.

The analysis of the effects of mineral composition in igneous rocks on their irradiated properties is discussed in the aforementioned work by the authors, as is the use of the simplified CBS model and the analysis of the effects of the rocks mineralogy on the structural performance.

2.1.1 Sedimentary Rocks

Sedimentary rocks are formed through the processes of transportation, deposition, compaction, cementation, and re-crystallization (i.e., diagenesis) of weathered rock fragments (i.e., clasts) and/or organic matter. In principle, all minerals present in the pre-weathered rock may be found in detrital grains.

The most common sedimentary rocks—including shale, sandstone, and conglomerate—are derived from siliciclastic sediments. The susceptibility of silicates to weathering varies according to Goldich's classification (Goldich 1938). For example, feldspar weathering leads to the formation of phyllosilicate minerals such as illite, chlorite, vermiculite, smectite, and kaolinite (Wilson 2004). Silicates that are less susceptible to weathering also exhibit greater tolerance to irradiation-induced damage (i.e., RIVE) (Le Pape, Alsaid, and Giorla 2018).

Other types of sedimentary rocks include carbonates (such as those found in limestones), iron oxides and hydroxides (e.g., hematite or goethite in iron formations), and other minerals.

Furthermore,

> "Quartz and clays are the main silicate minerals in most clastic rocks. Feldspars and sometimes muscovite may also be present but are usually subordinate to quartz. They are absent from rocks formed from sediments transported long distances or weathered for long times. Mafic silicate minerals (Fe and Mg bearing silicates) are exceptionally rare in sediments or sedimentary rocks. Besides quartz and clays, other silicates, including zeolites, may occasionally be present. Important non-silicate minerals in clastic rocks include carbonates, sulfates, oxides, halide minerals and occasionally pyrite." (Perkins 2022)

The following list outlines the results of three separate studies that have attempted to quantify the mineral content in sedimentary rocks.

1. Japan Concrete Aging Management Program (JCAMP) data (Maruyama et al. 2016): Table 1 and Table 2 provide the description of the rocks and their mineral compositions, respectively.

2. Russian data (Denisov, Dubrovskii, and Solovyov 2012): (IMAC ID: 28) Fine-grain laminated aleurolite (ϕ = 15%) – olivine 60%, serpentine 40%; (IMAC ID: 29) Small-grain sandstone – olivine 60%, serpentine 40%; (IMAC ID: 30) Fine-grain limestone (ϕ = 16%) – calcite: 99%; (IMAC ID: 31) Small-grain limestone – calcite 99%; (IMAC ID: 32) Fine-grain limestone (ϕ = 7%) – calcite 80%, dolomite 20%; (IMAC ID: 33) Medium-grain porous magnesite rock (ϕ = 7%) – magnesite 99%; (IMAC ID: 34) Fine-grain porous siderite rock (ϕ = 10%) – siderite 90%, quartz 10%; (IMAC ID: 35) Medium-grain dolomite rock – dolomite 95%, siderite 5%.

3. Sampled compositions assuming the constraints given in (Folk 1980). The sedimentary minerals are classified as terrigenous minerals–bearing or chemical mineral–bearing. "Terrigenous minerals are derived from erosion of source lands; comprise 60% to 80% of the stratigraphic column. The chemical minerals refer to the precipitation from solution within the basin of deposition; comprise 20% to 40% of the stratigraphic column." The expected terrigenous and chemical minerals abundances are detailed in Table 3 and **??**, respectively. Using the mineral composition's range constraints provided by Folk (1980), a set of randomly defined sedimentary rocks are created.

Table 1. JCAMP irradiated aggregates' types (sedimentary rocks) and origins.

Label	Type	Origin
GB	Felsic sandstone / Gravel	Shinozuka prefecture
GC	Felsic sandstone / Crushed	Tokyo
GD	Felsic sandstone / Crushed	Shinozuka prefecture
GE	Felsic sandstone / Crushed	Saitama prefecture
GF	Limestone / Crushed	Ooitta prefecture

Table 2. X-ray diffraction (XRD) Rietveld analysis of the aggregate-forming minerals (Maruyama et al. 2017). The range in variation of the volume fractions is estimated at ±1.5%. Qz: quartz, Ab: albite, An: anorthite, Ano: anorthoclase, Or: orthoclase, Mc: microcline, Chl: chlorite, Itl: illite, Ser: sericite, Bt: biotite, Cal: calcite, Dol: dolomite, Py: pyrite – Abbreviations according to Whitney and Evans (2010). † The remaining phase was classified as amorphous by (Maruyama et al. 2017).

		Feldspars					Phyllosilicates				Carbonates		
	Qz	Ab	An	Ano	Or	Mc	Chl	Ilt	Ser	Bt	Cal	Dol	Py
GB	0.47	0.24	0.07			0.05	0.03	0.04	0.10				
GC	0.40	0.29		0.03	0.03	0.09	0.04		0.07		0.03		0.03
GD	0.40	0.29		0.04	0.03		0.03	0.04	0.07				
GE	0.24	0.34					0.11		0.13		0.18	<0.01	
GF											0.91†		

Table 3. Relative abundance of minerals in terrigenous sedimentary rocks adapted from Folk (1980) and corresponding assumptions made in this study.

minerals	modeled as	weight fraction
quartz	quartz	0.35–0.50
clay minerals (Authigenic alteration common). Main types: sericite (impure fine grained muscovite), illite group, montmorillonite group, chlorite group (with Si low, FeMg high), kaolin group, bauxite group.	muscovite	0.25–0.35
metamorphic group fragments (not a mineral; includes detrital particles of slate, phyllite, schists, metaquartzite)	quartz ($f \in [0;1]$), muscovite $(1-f)$	0.05–0.15
feldspar (alkali feldspar considerably more abundant than plagioclase)	microcline, orthoclase	0.05–0.15
chert (mostly reworked from older cherty limestones)	(vitreous) silica	0.01–0.04
coarse mica (muscovite by far most common; some biotite and chlorite)	muscovite	0.001–0.004
carbonate (reworked fragments of older limestones)	calcite	0.012–0.02
accessory (heavy) minerals Opaques: magnetite, ilmenite, hematite, limonite and leucoxene. Ultrastable group: zircon, tourmaline, rutile. Less stable group: garnet, apatite, kyanite, staurolite, epidote, hornblende, pyroxene and about a hundred others of minor importance volumetrically.	magnetite	0.001–0.01

Table 4. Relative abundance of minerals in chemical sedimentary rocks adapted from Folk (1980) and corresponding assumptions made in this study. † Because of their ionic nature, they are assumed not to be susceptible to RIVE.

minerals	modeled as	weight fraction
carbonates calcite 2/3 to 3/4; dolomite 1/4 to 1/3; aragonite, siderite, ankerite minor	calcite, dolomite	0.70–0.85
silica (mostly quartz and chert; a little opal)	quartz ($f \in [0;1]$), vitreous silica $(1-f)$	0.10–0.15
sulfates and salts (Chiefly gypsum, anhydrite, halite; some sylvite and other potassium salts; a little barite, etc.)	halite †	0.02–0.07
miscellaneous (Feldspar, hematite, limonite, leucoxene, pyrite,** phosphates, glauconite, manganese, tourmaline, zircon, rutile, anatase, zeolites and many others)	microcline, hematite, pyrite, rutile	0.02–0.07

2.2 PROPERTIES OF IRRADIATED CONCRETE CONSTITUENTS

2.2.1 Aggregate-Forming Minerals

2.2.1.1 Radiation-Induced Volumetric Expansion

The RIVE of rock-forming minerals varies greatly with their chemical compositions. The analysis of post–neutron irradiation dimensional changes (Denisov, Dubrovskii, and Solovyov 2012; Le Pape, Alsaid, and Giorla 2018) and molecular dynamics (MD) simulations (Pignatelli et al. 2016; Wang et al. 2017; Krishnan et al. 2018, 2019) show that the range of maximum expansion—or, in some cases, contraction, such as with vitreous silica (Mayer and Lecomte 1960)—varies from a few per thousand (e.g., with carbonates) up to 17.8% in quartz. The main parameters governing the maximum expansion are the silica content, the ratio of ionic-to-covalent bonds, the dimensionality of SiO_4 polymerization (DOSP), the relative number of Si−O bonds per unit cell, and the relative bonding energy (RBE), which is the bonding energy normalized by that of quartz per unit cell (Keller 1954).

The RIVE of minerals is generally described as a function of the cumulative displacement per atom–induced amorphization, which depends on the cumulative fluence (Φ) at $E > 10$ keV and the irradiation temperature (T), which governs the annealing rate. Isothermal RIVE can be represented by sigmoidal (Zubov and Ivanov 1966) or piecewise linear empirical curves for individual minerals:

$$\tilde{\varepsilon}_i^* = \mathcal{F}_i(\Phi, T). \tag{1}$$

Here, $\mathcal{F}_i$ is a monotonic function dependent on the mineral. The function $\mathcal{F}_i$ is governed by a set of best-fit parameters (Le Pape, Alsaid, and Giorla 2018) calibrated using the Levenberg–Marquardt (Levenberg 1944; Marquardt 1963) technique to minimize the function $\sum_j |\tilde{\varepsilon}_i^(\Phi_j, T_j) - \varepsilon_i^(\Phi_j, T_j)|$, where $\varepsilon_i^*(\Phi_j, T_j)$ is the experimental data collection found in Denisov, Dubrovskii, and Solovyov (2012). Details of the parameter identification can be found in Le Pape, Alsaid, and Giorla (2018).

2.2.1.2 Elastic Properties

Pristine rock–forming minerals are assumed to be in the form of pure crystals or fully vitreous forms. Their elastic properties are obtained from acoustic wave propagation or resonance techniques, and MD simulations are well documented in the literature. The averaged unirradiated elastic constants at room temperature for 43 common rock–forming minerals are reported in the appendix of Le Pape, Sanahuja, and Alsaid (2020), compiling data from 83 peer-reviewed articles. The elastic properties of neutron-irradiated rock-forming minerals are poorly characterized, except for those of quartz (Mayer and Gigon 1956; Mayer and Lecomte 1960). Because neutron irradiation causes the gradual disordering of the crystal structure, the elastic tensor evolves toward an isotropic system.

Individual constants evolve differently and sometimes in a non-monotonic manner with increasing fluence for irradiated quartz. The exact evolution of these constants for minerals other than quartz is not well understood. Interpretations of MD simulations of various irradiated minerals (mostly silicates) have shown that the Young's modulus of an equivalent polycrystalline assemblage with randomly distributed orientations can be approximated by a cubic function of the density change (Krishnan et al. 2018). In the present study, the effects of irradiation on the elastic properties of minerals are implicitly accounted for in the empirical estimates of the aggregate properties.

2.2.2 Aggregate

2.2.2.1 Radiation-Induced Volumetric Expansion

The aggregate RIVE is the sum of the contributions from the rock-forming minerals, given by $\varepsilon^*_{a,u} = \sum f_i \varepsilon^*_i$ (where f_i is the volume fraction of mineral i), plus the formation of additional voids or cracks, denoted as $\Delta\phi$: $\varepsilon^*_a = \varepsilon^*_{a,u} + \Delta\phi$. $\varepsilon_{a,u}$ describes the volume change in uncracked irradiated aggregate. Estimating $\Delta\phi$ is more challenging because crack initiation is governed by the local stress field, which depends on the rock microstructure, and crack propagation is influenced by the fracture properties at the boundaries of mineral grains or within the grains themselves. In this study, $\Delta\phi$ was not considered because of a lack of sufficient data. Hence, the volumetric change of the aggregate is likely underestimated. To account for epistemic uncertainty in the minerals' RIVE models and to address the lack of consideration for irradiation-induced cracking, an uncertainty parameter, denoted as ξ_a, was introduced in the calculation of the aggregate RIVE:

$$\varepsilon^*_{a,u} \sim \xi_a \sum f_i \varepsilon^*_i \,, \tag{2}$$

where ξ_a ranges between 0.9 and 1.1.

2.2.2.2 Elastic Properties

The unirradiated Young's modulus of aggregate depends on the mineralogy of the rocks and the presence of defects such as small porosities or altered bonds between mineral grains. Theoretical estimates of the Young's modulus of mineral assemblages can be obtained through the average field homogenization theory of randomly distributed phases and crystalline orientations. In this work, the Young's modulus of the pristine aggregates was calculated using the Voigt–Reuss–Hill (VRH) estimates (Voigt 1889; Reuss 1929; Hill 1952): $\mathcal{E}(f_i, \mathbf{C}_i)$ where f_i is the volume fraction of mineral i, and $\mathbf{C}_i$ the corresponding stiffness tensor. In general, for silicated rocks, the estimates range between $\approx$ 80 and 105 GPa. These values are quite high compared to the limited experimental data on concrete aggregate. The present model assumes that the Young's modulus of the pristine aggregate is obtained by multiplying the VRH estimates by a correction factor, noted as κ^0_a, ranging from 0.6 to 0.7.

$$E^0_a \sim \kappa^0_a \mathcal{E}(f_i, \mathbf{C}_i) \,. \tag{3}$$

Two factors affect the elastic properties of irradiated rocks: the amorphization-induced change in the minerals' crystalline properties (Mayer and Gigon 1956; Mayer and Lecomte 1960; Krishnan et al. 2018) and the formation of voids and cracks. Predictive models for void and crack formation are not available at this writing. However, their effects on the Young's modulus of irradiated rocks can be captured through empirical relations linking the loss of modulus to the RIVE of the aggregate. Generally, the Young's modulus decreases with increasing RIVE (Denisov, Dubrovskii, and Solovyov 2012).

Figure 1 presents the experimental data collected from Denisov, Dubrovskii, and Solovyov (2012) and Maruyama et al. (2017) and the data produced by the LWRS Program (M3LW-22OR040303: Tajuelo et al. [2022] ORNL/TM-2022/2589). Although the irradiated modulus of igneous rocks (gray marks) exhibits a rapid decrease that can be fitted with an exponential law, the loss of Young's modulus in irradiated terrigenous sedimentary rocks follows a gentler decreasing trend , as shown by the red $*$ marks from Denisov, Dubrovskii, and Solovyov (2012) and colored marks—except for the red circles, which correspond to a metachert from JCAMP data.

It is assumed that the aggregate's loss of Young's modulus is modeled by a linear trend:

$$E^*_a \sim E^0_a \left(1 - \kappa^*_a \varepsilon^*_{a,u}\right) \,, \tag{4}$$

with κ^*_a ranging between 0.0509 and 0.0788.

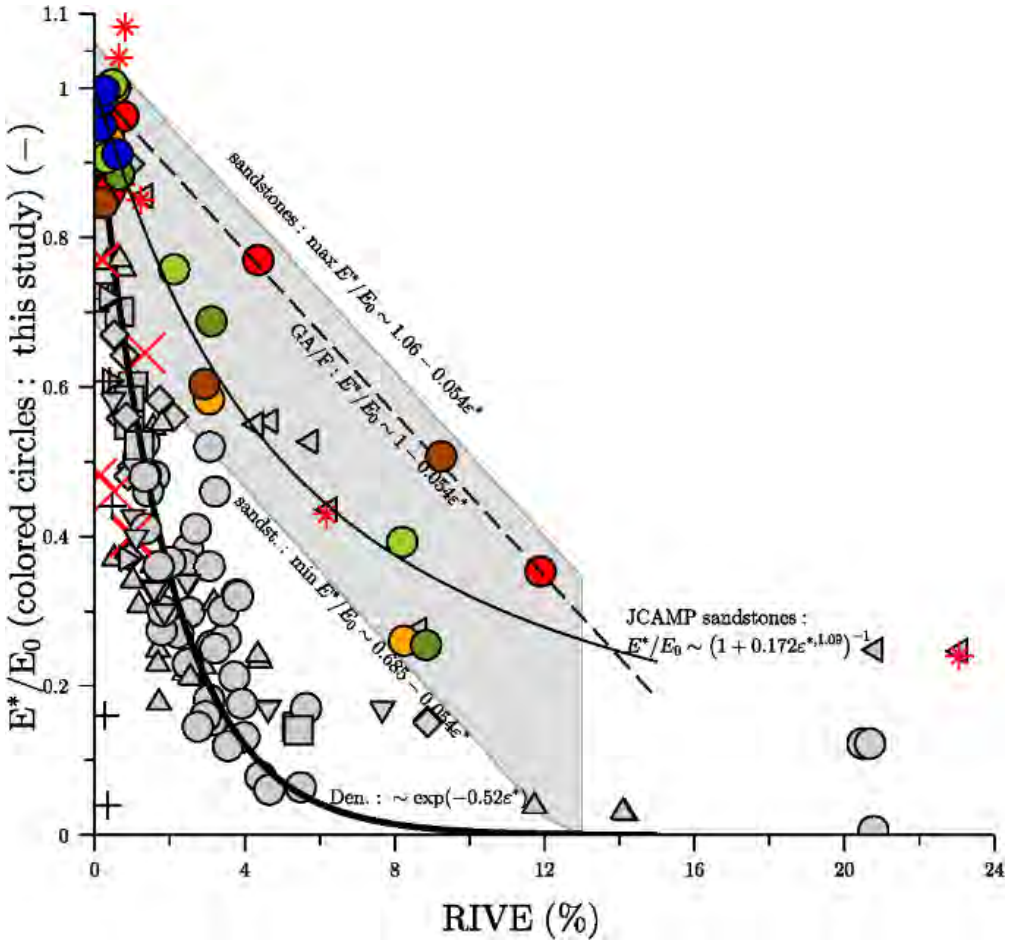

Figure 1. Loss of Young's modulus in irradiated rocks. Colored circles: JCAMP data; Gray/red marks: literature data from Denisov, Dubrovskii, and Solovyov (2012); upward triangles: albitite; left triangles: aleurolite; diamonds: diabase; circles: granite; squares: hornblendite; ×: limestone; right triangles: magnesite; downward triangles: pyroxenite; ∗: sandstone and +: siderite.

2.2.3 Hardened Cement Paste

2.2.3.1 Shrinkage

Cement paste subjected to irradiation exhibits shrinkage (Gray 1971; Elleuch, Dubois, and Rappeneau 1972; Maruyama et al. 2017) caused by moisture transport–induced heating. At the operating temperatures of light-water reactors (LWRs) (i.e., < 65 °C), the value of shrinkage is assumed to be around $\tilde{\varepsilon}_m^{sh} \sim 0.1\%$.

2.2.3.2 Elastic Properties

For the purpose of this research, the elastic properties for the hardened cement paste were assumed to be constant: $E_m \approx 5$ MPa (delayed/long-term equivalent modulus (Le Pape, Field, and Remec 2015)) and $\nu_m \approx 0.2$.

2.2.4 Concrete

2.2.4.1 Radiation-Induced Volumetric Expansion, Thermal Strains, and Shrinkage

Concrete dimensional change includes the contribution of the aggregate RIVE, the cement paste shrinkage, and the thermal expansion of both constituents. The coefficient of thermal expansion of cement paste varies between $\alpha \approx 15$ and 25×10^{-6} °C^{-1} with the hydration degree and the moisture content (Sellevold and Bjontegaard 2006; Maruyama, Teramoto, and Irashi 2014). The volume fraction of aggregates is denoted by f_a, and its value ranges between 0.65 and 0.80. The analysis of the data provided by Elleuch, Dubois, and Rappeneau (1972) and Gray (1971) led to the conclusion that the concrete RIVE can be approximated by two 'loose' bounds:

$$\tilde{\varepsilon}_c^{(i)} = f_a \tilde{\varepsilon}_a + (1 - f_a)\, \tilde{\varepsilon}_m^{sh} \text{ and } \tilde{\varepsilon}_c^{(ii)} = \frac{2 f_a}{1 + f_a} \left(\tilde{\varepsilon}_a + \tilde{\alpha} \Delta T\right), \tag{5}$$

where $\tilde{\varepsilon}_c^{(i)}$ is an approximation of the concrete RIVE for an uncracked cement paste when the elastic properties of the irradiated aggregates and the cement pate are comparable; $\tilde{\varepsilon}_c^{(i)}$ includes the contribution of the cement paste shrinkage $\tilde{\varepsilon}_m^{sh}$; and $\tilde{\varepsilon}_c^{(ii)}$ corresponds to the situation of a fully damaged cement paste. With a typical aggregate volume fraction of 0.60 to 0.75, $2f_a/(1 + f_a)$ varies in the range of 0.75–0.80. Drying shrinkage is a function of moisture transport. In LWRs' CBSs, moisture transport is influenced by exchange conditions, such as the presence or absence of a metal liner, a venting system, and the air gap in the reactor cavity, as well as by the radiolysis of water. As previously mentioned, a default value of 0.1% was assumed for shrinkage.

In the CBS model, the volumetric strains caused by shrinkage, thermal expansion, and RIVE was calculated using the average value of $\tilde{\varepsilon}_c^{(i)}$ and $\tilde{\varepsilon}_c^{(ii)}$:

$$\tilde{\varepsilon}_c = \frac{1}{2}\left(\tilde{\varepsilon}_c^{(i)} + \tilde{\varepsilon}_c^{(ii)}\right). \tag{6}$$

2.2.5 Elastic Properties

Concrete is modeled using a Hashin composite sphere (Le Pape, Field, and Remec 2015). The effective bulk modulus of concrete $\tilde{k}_c$ is

$$\tilde{k}_c = \tilde{k}_m + \frac{f_a \left(\tilde{k}_a - \tilde{k}_m\right)}{1 + (1 - f_a)\frac{\tilde{k}_a - \tilde{k}_m}{\tilde{k}_m + \frac{4}{3}\tilde{\mu}_m}}, \tag{7}$$

and the effective shear modulus $\tilde{\mu}_c$ is

$$\tilde{\mu}_c = \tilde{\mu}_m + \frac{f_a \left(\tilde{\mu}_a - \tilde{\mu}_m\right)}{1 + (1 - f_a)\left[\frac{\tilde{\mu}_a - \tilde{\mu}_m}{\tilde{\mu}_m + \frac{\tilde{\mu}_m(9\tilde{k}_m + 8\tilde{\mu}_m)}{6(\tilde{k}_m + 2\tilde{\mu}_m)}}\right]}, \tag{8}$$

where f_a is the volume fraction of aggregates. The subscripts $_m$ and $_a$ denote the properties of the cement paste and the aggregates, respectively. The Young's modulus and the Poisson's ratio are given by $E_c = 9k_c\mu_c m/(3k_c + \mu_c)$ and $\nu_c = \frac{1}{2}(3k_c - 2\mu_c)/(3k_c + \mu_c)$.

2.2.5.1 Strength

2.2.5.2 Tensile Strength

The tensile strength of concrete decreases with fast neutron fluence exposure (Hilsdorf, Kropp, and Koch 1978; Field, Remec, and Le Pape 2015). In the context of this study, the final objective is to assess the effects of aggregates' chemical composition on the depth of irradiation-induced damage. Based on the results of a sensitivity analysis, it was concluded that the tensile strength of irradiated concrete has very limited influence on the damage depth. This is explained by the stress state in the concrete near the reactor cavity: RIVE mainly causes biaxial stresses in the vertical and the orthoradial direction. Thus, from a limit state point of view, the tensile strength of irradiated concrete is not a parameter of first-order importance. A default value of 4 MPa was used in this study.

2.2.5.3 Compressive Strength

The compressive strength of irradiated concrete decreases significantly when exposed to fast neutron fluences above 10^{19} n·cm^{-2} (Hilsdorf, Kropp, and Koch 1978; Field, Remec, and Le Pape 2015). The loss of resistance is associated with a reduction in the strength of the aggregates and possibly with crack formation due to excessive aggregate RIVE. It can be hypothesized that the compression failure mode may vary depending on the level of irradiation-induced damage in the aggregates. At low fluences, compression failure may primarily occur in the cement paste and around the aggregates, similar to typical failure modes observed in ordinary concrete with natural aggregates. However, at higher fluences, the degradation of the mechanical properties of the aggregates may lead to trans-aggregate fractures.

Homogenization schemes of such complex fracture problems are quite ineffective. Thus, an empirical model was adopted for this study. Using the data published by Denisov, Dubrovskii, and Solovyov (2012) and shown in Figure 2, the loss of compressive strength of irradiated concrete can be estimated from its dimensional change:

$$f_c^*/f_c^0 \sim \begin{cases} \min[1; \exp(-65(\varepsilon^*))] & \text{lower bond} \\ \min[1; 1.20 - 14.5\varepsilon^*] & \text{upper bond} \end{cases}. \tag{9}$$

In the simulation of the CBS presented in this report, the lower bound was adopted to obtain conservative estimates. The value f_c^0 is constant at 40 MPa.

2.2.6 Summary

The main equations governing the properties of concrete constituents are summarized in this section. In the CBS calculations presented in Section 2.3, some parameters are considered variable. Aleatory and epistemic parameters are shown in red and blue fonts, respectively, in the equations. These equations allow for the propagation of variability in the chemical composition of concrete aggregates through to the concrete level under different irradiation conditions.

2.2.6.1 Irradiated Aggregate Properties

The composition of a terrigenous sedimentary aggregate was modeled by the volume fractions (f_i) of quartz, muscovite, microcline, silica, calcite and magnetite. For a given fast neutron fluence Φ and temperature T, the aggregate RIVE is defined by:

$$\varepsilon_{a,u}^* =\sim \xi_a \sum f_i \varepsilon_i^*(\Phi, T). \tag{10}$$

The aggregate's Young's modulus at the corresponding irradiation conditions is formulated as follows:

$$E_a^* \sim \kappa_a^0 \mathcal{E}(f_i, \mathbf{C}_i)\left(1 - \kappa_a^* \varepsilon_{a,u}^*\right). \tag{11}$$

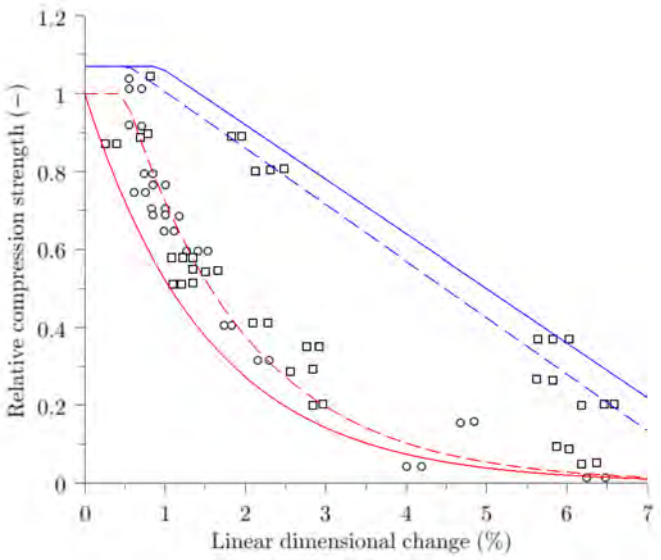

Figure 2. Irradiated concrete (□) and mortar (○) relative strength (f_c^*/f_c^0). Upper envelope curves: (blue dashed line) $\min[1; 1.15 - 14.5\varepsilon^*/3]$; (blue solid line) $\min[1; 1.20 - 14.5\varepsilon^*]$. Lower envelope curves: (red dashed line) $\min[1; \exp\left(-65(\varepsilon/3)\right)]$; (red solid line) $\min[1; \exp(-65(\varepsilon^*/3 - 0.5\%))]$ with ε^* the RIVE in percent.

2.2.6.2 Concrete Properties

The volumetric expansion of concrete caused by aggregate RIVE ($\varepsilon^*_{a,u}$), shrinkage in the cement paste ($\tilde{\varepsilon}^{sh}_m$), and thermal expansion ($\alpha\Delta T$), is calculated using Eq. (6), which can be written using a compact form as

$$\tilde{\varepsilon}_c \sim \mathcal{G}\left(f_a, \varepsilon^*_{a,u}(f_i, \Phi, T), \tilde{\varepsilon}^{sh}_m, \alpha\Delta T\right). \tag{12}$$

The elastic properties of concrete are obtained using Hashin's composite sphere model—Eqs. (7) and (8):

$$[\tilde{E}_c, \tilde{\nu}_c] \sim \mathcal{H}\left(f_a, \tilde{E}_m, \tilde{\nu}_m, \kappa^0_a \mathcal{E}(f_i, \mathbf{C}_i)\left(1 - \kappa^*_a \varepsilon^*_{a,u}\right)\right). \tag{13}$$

The compressive strength of concrete varies with the concrete RIVE:

$$f_c^* \sim f_c^0 \min[1; \exp(-65\tilde{\varepsilon}_c)]. \tag{14}$$

2.3 1D CBS MODEL

2.3.1 Model Features

The previous section describes the constitutive models governing the properties of concrete subjected to fast neutron irradiation. This section analyzes the effects of irradiation on the degradation of a prototypical PWR CBS. A detailed simulation of an irradiated CBS requires intensive computational resources using finite element models (Pomaro et al. 2011; Khmurovska et al. 2019; Cheniour et al. 2023) or discrete structural models (Kambayashi et al. 2020). For this study, a simplified approach was adopted. It is based on a nonlinear finite difference 1D model published in Le Pape (2015). The main assumptions and features of the 1D simplified CBS are as follows.

1. The 1D radial model provides a representation of the CBS wall directly facing the reactor pressure vessel (RPV) belt line. The displacement field is a function of the radius $u(r, \theta, z) = u_r(r)$ only.

2. The steel reinforcement was not modeled (plain concrete model only).

3. The vertical strains were assumed to be negligible. This assumption is considered conservative because it maximizes the RIVE-induced compression stress in the vertical direction.

4. Concrete properties account for the effects of irradiation. In the 2015 model, those properties were simply fitted to a collection of irradiated concrete data published in Field, Remec, and Le Pape (2015). Each property was simply assumed as a function of the fast neutron fluence, without any distinction made on the composition of the concrete or the chemical composition of the aggregates. In this study, the irradiated properties of the concrete were calculated using the expression provided in Section 2.2. Therefore, the irradiated concrete properties vary with r as functions of the fast neutron fluence and irradiation temperature.

5. Additional damage caused by excessive mechanical stresses such as that described by Mazars and Pijaudier-Cabot (1989) is not accounted for. Local force equilibrium, $\partial\sigma_r/\partial r + (\sigma_r - \sigma_\theta)/r = 0$, yields the following after calculation to the ordinary differential equation (ODE):

$$\tilde{M}_c \frac{\partial^2 u}{\partial r^2} + \left(\frac{\partial \tilde{M}_c}{\partial r} + \frac{\tilde{M}_c}{r} \right) \frac{\partial u}{\partial r} + \left(\frac{\partial \lambda_c}{\partial r} - \frac{\tilde{M}_c}{r} \right) \frac{u}{r} - 3 \frac{\partial}{\partial r} \left(\tilde{k}_c \tilde{\varepsilon}_c \right) = 0, \tag{15}$$

   where $\tilde{M}_c$ is the P-wave modulus of concrete, that is, $\tilde{M}_c = \tilde{k}_c + 4\tilde{\mu}_c/3 = \tilde{E}_c(1 - \tilde{\nu}_c)/(1 + \tilde{\nu}_c)/(1 - 2\tilde{\nu}_c)$, and $\tilde{\lambda}_c$ is Lamé's first parameter—$\tilde{\lambda}_c = \tilde{k}_c - 2\tilde{\mu}_c/3$. The elastic properties ($\tilde{M}_c$, $\tilde{k}_c$, $\tilde{\lambda}_c$) and the imposed strain $\tilde{\varepsilon}_c$ vary along the radius because the irradiation conditions are also variable with the radius.

6. The neutron and gamma irradiation fields used in this analysis were simulated—see Remec et al. (2014) and Field, Remec, and Le Pape (2015) for details—using the DORT computer code from the DOORS3.2a code system. Based on preliminary theoretical analysis performed at Oak Ridge National Laboratory (Remec et al. 2014) on simple crystalline forms of minerals, fast neutrons above 0.1 MeV and 10 keV are suspected to develop, respectively, ≈95% and ≈ 100% of the total damage (displacements per atom equivalent). The specific neutron flux profile used as input data for the subsequent calculations was obtained by the modeling of a Westinghouse 3-loop PWR design. In this study, a fluence of 0.6 n·pm^{-2} ($E > 10$ keV) at the surface of the CBS was assumed. The temperature profile was derived from the heat transfer simulation accounting for the heat generated by gamma and neutron irradiation, that is, solving the steady-state ODE: $\frac{1}{r}\frac{\partial}{\partial r}\left(Kr\frac{\partial T}{\partial r}\right) + Q_{\gamma,\Phi}(r) = 0$. Gamma and neutron heating profiles $Q_{\gamma,\Phi}(r)$ were obtained as outputs of DORT computer code simulations. The calculated fluence and temperature profiles are presented in Figure 3.

7. The objective of the proposed structural integrity analysis is to evaluate the risk of stress-induced cracking, as well as the potential location and orientation of the cracks by a comparison with the soliciting stress fields and the admissible stresses (i.e., failure criterion) defined by the strength of concrete. The radiation swelling–induced stress state is essentially biaxial: highly solicited areas are prone to prominent orthoradial and vertical stresses. The radial stresses are about one order of magnitude lower than the other stresses (elastic analysis) in those regions (Le Pape 2015). Thus, a biaxial failure criterion $g(\sigma'_1, \sigma'_2, f_c, f_t) = 0$ based on experimental data from Kupfer, Hilsdorf, and Rüsch (1969) was adopted:

$$\text{if } \sigma'_2 \geq \sigma'_1 \geq 0 : \sigma'_2 - f_t = 0, \tag{16}$$

$$\text{if } \sigma'_2 \geq 0 \text{ and } \sigma'_1 \leq 0 : \frac{\sigma'_2}{f_t} - \xi\frac{\sigma'_1}{f_c} - 1 = 0, \tag{17}$$

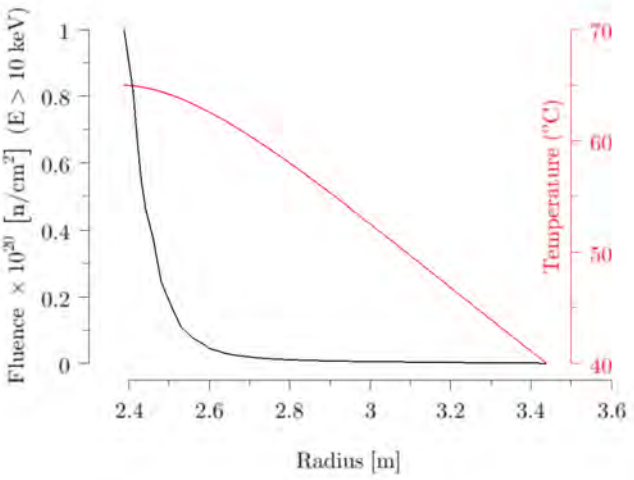

Figure 3. Fast neutron fluence and temperature profiles used as inputs for the CBS 1D simulation.

$$\text{if } \sigma'_1 \leq \sigma'_2 \leq 0 : \left(\frac{\sigma'_2}{f_c} + \frac{\sigma'_1}{f_c}\right)^2 + 3.65\frac{\sigma'_2}{f_c} + \frac{\sigma'_1}{f_c} = 0, \tag{18}$$

where σ'_1 and σ'_2 are the ultimate principal stresses in the loaded plane. The relations above are given for the half-plane defined by $\sigma'_2 \geq \sigma'_1$. Similar relations describing the failure function in the second half plane are simply obtained by switching indices $_1$ and $_2$. The domain defined by Eqs. (16–18) corresponds to a Rankine criterion in tension (Rankine 1857) and a capped criterion in compression. $\xi = 0.8$ provides the best fit with the experimental values (Kupfer, Hilsdorf, and Rüsch 1969). Here, for the sake of simplicity, ξ was taken to be equal to 1.0, which corresponds to a slightly more conservative failure criterion in the tension–compression regime. When the stress state remains within the boundary of the inner domain defined by $g \leq 0$, concrete is assumed to be undamaged, whereas when the local stress exceeds the mechanical resistance of concrete, $g > 0$, cracking is expected. When tensile, brittle mode is envisioned, $g > 0$ indicates the loss of resistance expected from that specific portion of the studied structure. Note that there are no data available in the literature on the failure properties of irradiated concrete under multiaxial loading. Here, it was simply assumed that Eqs. (16-18) hold when the tensile and compressive strengths decrease with the neutron irradiation (See Figure 4).

8. The main output of the simulation is the radiation-induced damage depth (RIDD). The RIVE-induced elastic stresses generally exceed the irradiated concrete resistance defined by the Kupfer's failure surface in the concrete area directly adjacent to the reactor cavity. The RIDD is defined by the depth of concrete subjected to excessive stresses (beyond failure with no residual structural resistance).

9. This study is limited to sedimentary terrigenous rocks. A similar study of igneous rocks was presented in the report titled "Effects of Aggregates Mineralogy on the Irradiation-Induced Damage in Concrete Biological Shields" (Le Pape, Sabatino, and Tajuelo Rodriguez 2023).

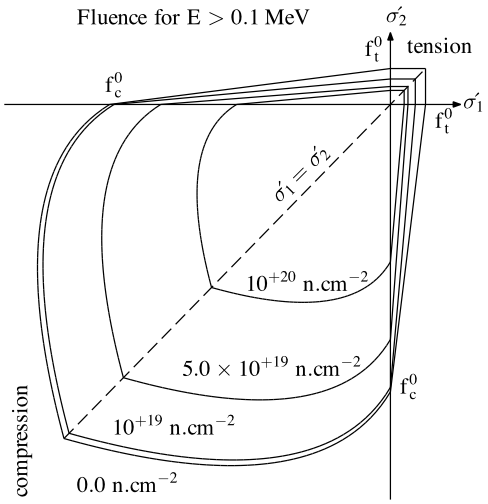

Figure 4. Failure criterion of irradiated concrete under biaxial loading based on Kupfer's function for unirradiated concrete (Kupfer, Hilsdorf, and Rüsch 1969). Reproduced from Le Pape (2015).

2.4 PROBABILISTIC ANALYSIS

The previous section of this report summarizes the procedure to calculate damage penetration depth within an irradiated prototypical PWR CBS, considering a set of predefined assumptions regarding the mineral composition, aggregate properties, and cement strength. This deterministic analysis may be expanded to a probabilistic study by considering various sources of uncertainty and performing the 1D CBS model calculations iteratively with varying inputs. In this context, uncertainties can be categorized as either aleatoric or epistemic. An aleatoric uncertainty is one that is attributed to the intrinsic randomness of a physical phenomenon, whereas an epistemic uncertainty is one that is propagated due to lack of knowledge or data. Aleatoric uncertainties are often introduced into a computational simulation by sampling a parameter (e.g., mineral composition, aggregate volume fraction, material strength) from a known probability distribution. Epistemic uncertainties are typically represented in a robust model by introducing non-physical random variables that quantitatively capture variances or unknowns in interdependencies/correlations (Der Kiureghian and Ditlevsen 2009).

This section of the report outlines the procedure to perform a probabilistic study on the damage penetration of the CBS. The deterministic analysis discussed in Section 2.3 was iteratively deployed, and input parameters were sampled from known probability distributions in order to represent various aleatoric and epistemic uncertainties. The output of these simulations is a set of damage penetration depths that can be further studied and characterized in a probabilistic context.

2.4.1 Input Random Variables

Various uncertainties are encountered at each level of the deterministic analysis proposed in previous sections. More specifically, the uncertainties at the mineral, aggregate, and concrete levels are considered in this novel

probabilistic study. For each uncertainty, a random variable or multiple random variables were introduced into the simulation.

Table 5 summarizes the random input variables for this simulation. In total, 12 input random variables were used in this exercise; random variables 1–7 are representative of mineral composition, the RIVE multiplier is quantified with random variable 8, random variables 9 and 10 represent the unirradiated and irradiated aggregate Young's modulus reduction factors, respectively, the aggregate volume fraction is quantified with random variable 11, and random variable 12 represents the coefficient of thermal expansion of the concrete. Model uncertainties (i.e., epistemic) are quantified within random variables 8–10, and inherit natural uncertainties (i.e., aleatoric) are represented by random variables 1–7, and 11–12.

Table 5. Probabilistic input variables: unirradiated and irradiated properties of concrete and concrete constituents.

Input variables	Value	Uncertainty and random variable (r.v.) number
Minerals		
Weight fractions	Uniform distributions See Table 3 for ranges	Aleatoric (r.v. 1–7)
Aggregate		
Volume fraction	$f_a \sim \mathcal{U}(0.65, 0.80)$	Aleatoric (r.v. 11)
RIVE	Eq. (10)	
	$\xi_a \sim \mathcal{U}(0.9, 1.1)$	Epistemic (r.v. 8)
Young's modulus	Eq. (3)	
	$\kappa_a^0 \sim \mathcal{U}(0.6, 0.7)$	Epistemic (r.v. 9)
	$\kappa_a^* \sim \mathcal{U}(0.0509, 0.0785)$	Epistemic (r.v. 10)
Poisson's ratio	0.2	Deterministic
Cement paste		
Young's modulus	5 MPa	Deterministic
Poisson's ratio	0.2	Deterministic
Shrinkage	0.1%	Deterministic
Concrete		
Shrinkage	100 $\mu m\,m^{-1}$	Deterministic
Coefficient of thermal expansion	$\tilde{\alpha} \sim \mathcal{U}(5, 15)$ $\mu m\,m^{-1}\,°C^{-1}$ (T_{ref} = 20 °C)	Aleatoric (r.v. 12)
Imposed strain	Eq. (6)	Deterministic
Young's modulus	Derived from Eqs. (7) and (8)	Deterministic
Poisson's ratio	idem	Deterministic
Compressive strength	Unirradiated: 40 MPa	Deterministic
	Relative residual strength of irradiated concrete Eq. (14)	Deterministic
Tensile strength	4 MPa	Deterministic

2.4.2 Output Random Variable

Using the deterministic procedure previously outlined in Section 2.3 with a sufficient number of samples of the 12 input random variables summarized in Table 5, a probabilistic study was carried out to quantify the effects of irradiation on the degradation of a prototypical PWR CBS composed of sedimentary terrigenous rocks. The output of the simulation is the penetration depth of damage, measured in units of length, normal

to the inner surface of the CBS. The iterative simulations were halted after approximately a week of run time, and 2,011 runs were recorded. Figure 5 depicts the output random variable, damage penetration, from 2,011 separate simulations, discretized into bins to form a histogram. Weibull and lognormal probability distribution functions (PDFs) were fit to these data and are shown in Figure 5 as black and red lines, respectively. The fitted Weibull distribution has scale and shape parameter values of 0.08061 and 10.89, respectively, whereas the fitted lognormal distribution has parameters (i.e., the mean and standard deviation of logarithmic values, respectively) equal to −2.572 and 0.1159. A visual comparison of these fitted PDFs with the histogram shown in Figure 5 confirms that both fitted distributions are relatively accurate probabilistic characterizations of the damage penetration depth data.

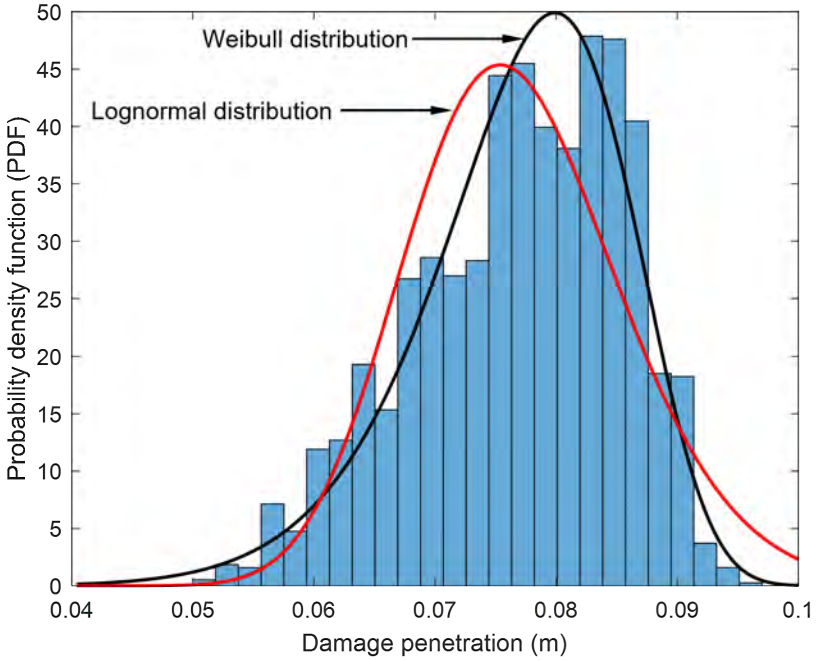

Figure 5. Histogram of damage penetration with Weibull distribution (black) and lognormal distribution (red) fit to the data.

To further analyze the fitness of the Weibull and lognormal PDFs, probability paper plots for each distribution were created and are shown in Figure 6. A probability paper is a visual tool that shows how well a particular probability distribution fits a data set. The ordered pairs plotted in these graphs have horizontal axis values equal to damage penetration and vertical axis values representative of the percentage of samples that possess an equal or smaller damage penetration depth. The vertical axes of probability paper plots are arranged such that a straight line indicates a perfect fit for a set of data. Figure 6(a) shows that the Weibull distribution, represented by the dashed black line, fits the data well for damage penetration depths greater than 0.06 m. Figure 6(b) shows that the lognormal distribution fits the data well for damage penetration depths less than 0.085m. The authors of this work believe that it is most important to capture the behavior on the right tail of the damage penetration depth distribution (i.e., the larger values, representative of the "worst-case" scenarios). Thus, considering the probability paper plots in Figure 6, the authors chose the Weibull distribution as the best fit for the damage penetration data.

To determine the significance of each of the 12 input random variables on the output random variable—that is, the damage penetration depth (i.e., random variable 13 in this simulation)—the correlations among all 13 random variables were calculated and are depicted as a heat map shown in Figure 7. The diagonal values in

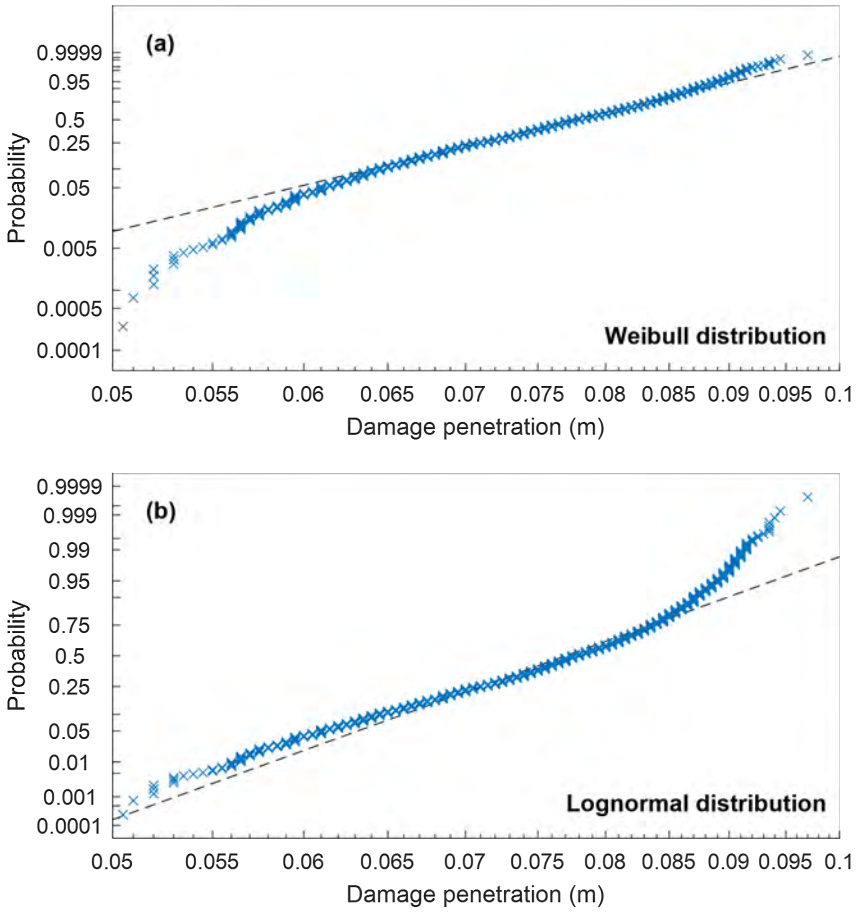

Figure 6. Probability paper plots for damage penetration considering the (a) Weibull and (b) lognormal distributions.

this correlation matrix are always equal to 1 because each random variable is directly correlated to itself. The off-diagonal terms in this matrix indicate the cross correlation among the different variables. In Figure 7, the most important or significant input variables have correlation values close to 1 (i.e., full positive correlation) or −1 (i.e., full negative correlation) when compared to the damage penetration (i.e., random variable 13). Using this criteria, random variables 11 (i.e., the aggregate volume fraction) and 13 were observed to have a correlation coefficient of 0.872, indicating a strong positive correlation between them.

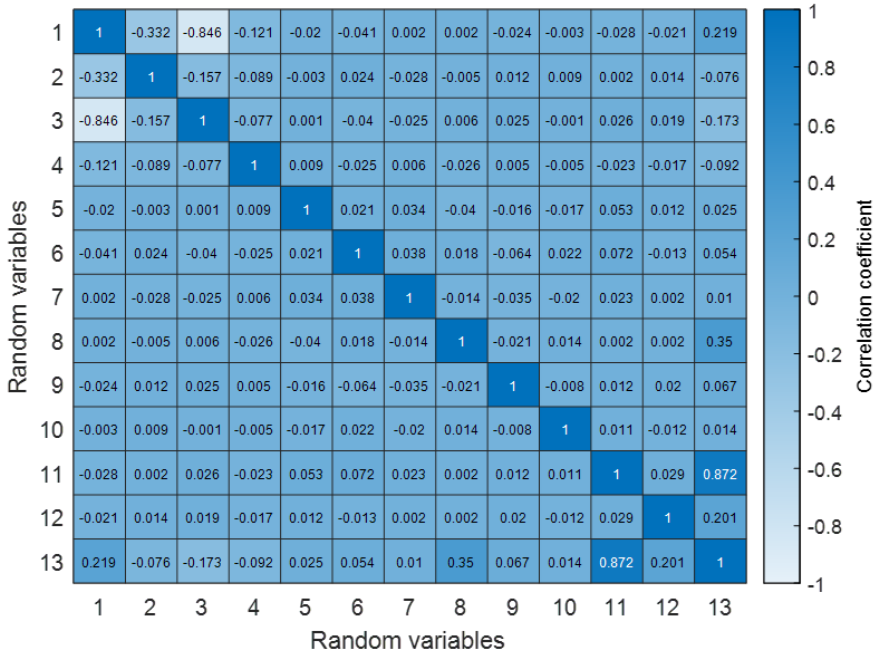

Figure 7. Correlation coefficient heat map for random variables considered in the probabilistic simulation; random variables 1–12 are the input variables, and random variable 13 is the damage penetration output.

To better understand the relationship between the aggregate volume fraction and the damage penetration, a scatter plot depicting the value of these two random variables for every sample is shown in Figure 8(a). This figure depicts a strong correlation between the damage penetration and aggregate volume fraction; relatively small aggregate volume fractions are paired with relatively small damage penetration depths, whereas relatively large aggregate volume fractions are paired with relatively large damage penetration depths. Furthermore, the samples may be discretized into bins with respect to damage penetration, and for each bin a mean aggregate volume fraction was calculated. The mean aggregate volume fraction associated with each bin of damage penetration is visually depicted as the shaded fill of each histogram bar in Figure 8(b). Figure 8(b) contains the same histogram shown in Figure 5 but with a fill color that corresponds to a mean aggregate volume fraction, as indicated by the vertical colorbar to the right of the graph. The black line in Figure 8(b) indicates the Weibull distribution previously fit to the data. Overall, Figure 8 visually confirms a strong correlation between the input random variable of aggregate volume fraction and the output random variable of damage penetration.

As a final step in this probabilistic study, the probability of damage reaching the steel rebar was calculated. Figure 9 shows the probability of the damage penetration extending beyond the rebar, located 3 in. from the inner surface of the CBS. This probability is calculated as the area underneath the PDF curve, indicated by the shaded blue region. To calculate this probability of exceedance, the Weibull cumulative distribution

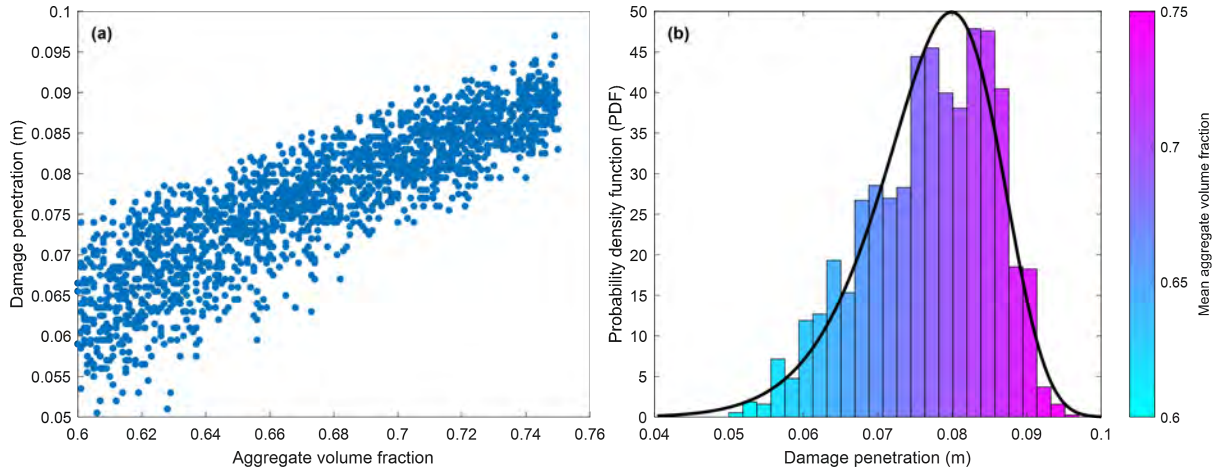

Figure 8. (a) Damage penetration vs. aggregate volume fraction for all samples and (b) damage penetration histogram with shaded bars indicative of mean aggregate volume fraction associated with each bin and fitted Weibull distribution (thick black line).

function at a penetration depth of 0.0762 m (i.e., 3 in.) is subtracted from 1. The probability that the damage reaches or extends beyond the rebar location is 0.5815, considering the results of this study. When the damage reaches the rebar location, this is indicative of the concrete cover no longer providing strength and the rebar being potentially exposed. Since the rebar cage provides the main structural integrity within the CBS, concrete cover spawling and exposure of rebar should be avoided. Note that this probability of exceedance is associated with a particular fluence level (i.e., 0.6 n·pm^{-2} ($E > 10$ keV) at the surface of the CBS). It would be prudent in future work to perform this probabilistic study to determine the probability of exceedance for different fluence levels.

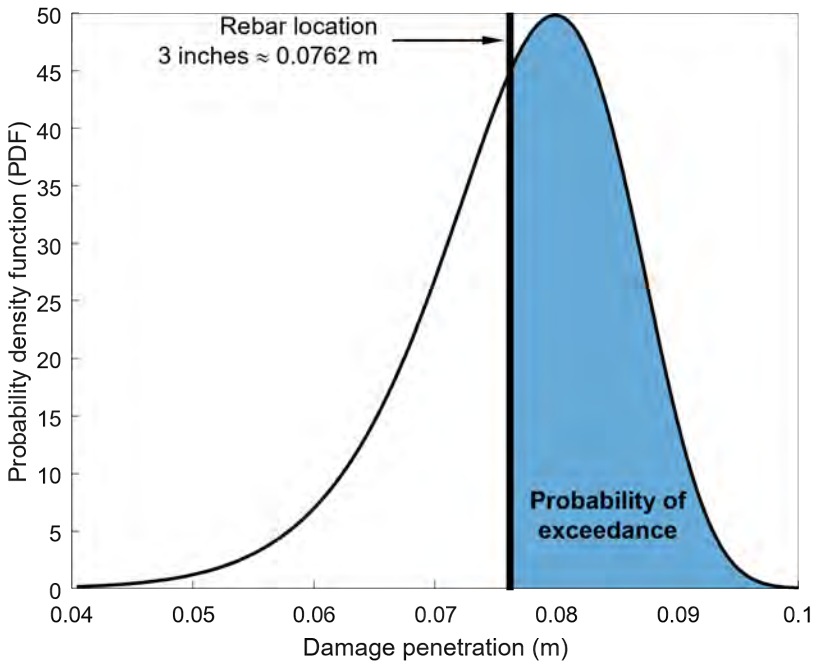

Figure 9. Probability of the damage penetration extending beyond the rebar location at 3 in. from the surface of the CBS.

3. NEUTRON-IRRADIATION CRACKING IN ROCK SPECIMENS

The Japanese rock specimens irradiated at the JEEP-II reactor have been extensively characterized by both the JCAMP team and ORNL. They comprise the sandstones with described mineralogical composition in Table 2, a tuff or meta-chert (GA) comprising 92% quartz, and a limestone (GF) mainly composed by calcite. Efforts to characterize neutron-induced cracks and quantify the crack volume have been carried out by both teams using techniques such as He pycnometry, conventional XCT, dimensional measurements and SEM imaging (Tajuelo Rodriguez et al. 2021; Maruyama et al. 2022; Maruyama et al. 2023).

Some discrepancies were found between the findings of both teams regarding aggregate GA, the composition of which was reported to be 92% quartz with minor amounts of feldspars and chlorite (Maruyama et al. 2017). Since this aggregate is very homogeneous in composition, differential expansion between the different minerals in this rock is expected to be minimal. XCT data by ORNL lacked good contrast to properly segment defects, and only minor voids were observed in the sample irradiated to a neutron dose of 8.25×0.1^{19} n·cm^{-2} ($E > 10$ MeV) (Figure 10).

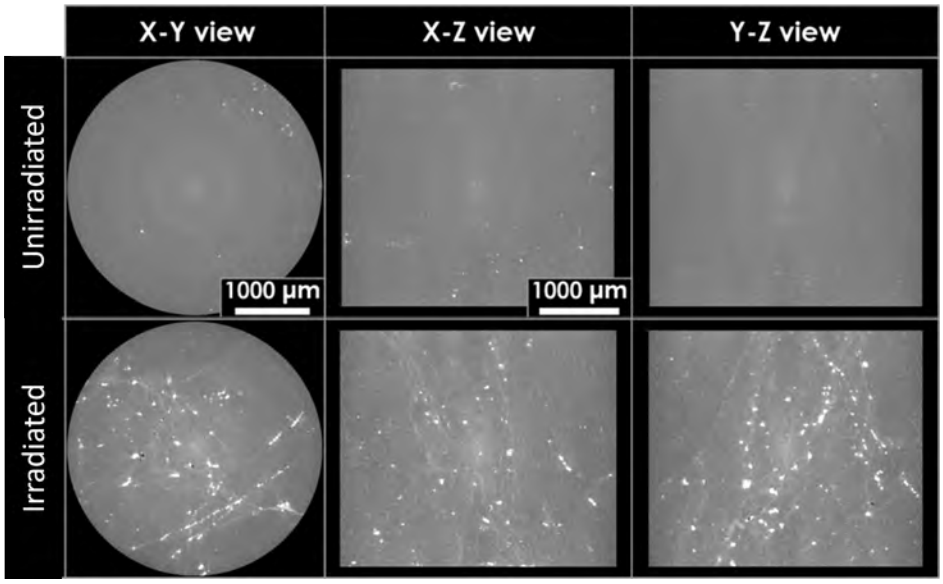

Figure 10. XCT of the pristine and irradiated GA samples showing voids in the irradiated specimen.

The JCAMP team prepared SEM samples for characterization of the cracks of this irradiated rock. They observed opening of the grain boundaries (Figure 11) and quantified the crack volume by analysis of the collected SEM images. The obtained volume was larger than that expected from the difference between the volumetric expansion measured by dimension inspection and He pycnometry (Maruyama et al. 2022). Several phenomena could account for this overestimation:

1. Opening of minor defects at grain boundaries due to the polishing required for SEM imaging
2. Analysis of a limited area that could have small quartz grains that are not representative of the bulk (this sample contains quartz grains of two distinct size groups)
3. Extrapolation of 2D quantified crack volume to 3D

To overcome these technical difficulties the ORNL team carried out some XCT scans using synchrotron micro-XCT. This imaging technique does not require sample preparation other than radiological sample containment.

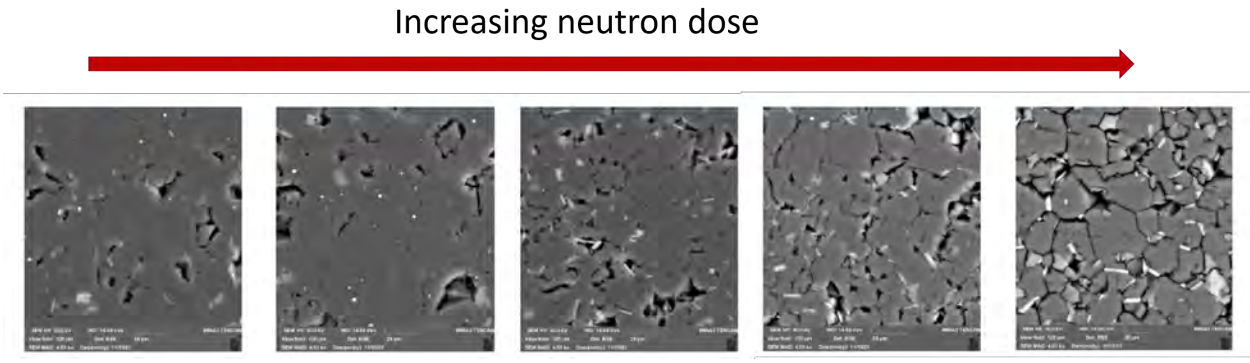

Figure 11. Opening of grain boundaries with increasing neutron dose for sample GA. Modified from Maruyama et al. (2022).

3.1 SYNCHROTRON MICRO-XCT

XCT scans with micron resolution were performed at the Advanced Photon Source (APS) at Argonne National Laboratory (ANL). The radiological specimens were covered in two layers of kapton to provide containment and to avoid contamination of the beam line hardware. The covered samples were then introduced in plastic vials as a secondary layer of containment. The vials were also wrapped in kapton tape (Figure 12). Pristine samples were mounted on the hardware table using Play-Doh, as were the irradiated samples on the vials. The scans were collected at beam line 13 BMD GSECARS, which is exclusively dedicated to geological specimens. This beam line offers advantages over conventional XCT by allowing the contrast to be more heavily focused on phase contrast rather than x-ray absorption contrast. Phase contrast is preferred in this case because the mineral phases in these samples are very close in density and will yield similar absorption contrast. Scans of 1.09 μm pixel size covering a volume defined by 2.1 mm in width and depth and 3.8 mm in height were collected on the pristine specimens and those irradiated to a dose of 8.25 x 10^{19} n·cm^{-2} (E > 10 MeV). The scans were collected in 3 sections that were stitched together using the IDL, a software for processing tomography data available at the beamline. The package tomo_display within IDL was created to allow the user to process and reconstruct parallel beam tomographic data, including removal of anomalous pixels, ring artifact reduction, and automated determination of the rotation center.

Figure 12. Encapsulation of an irradiated specimen with double layer of kapton tape, plastic vial, and external kapton tape.

3.2 IMAGE PROCESSING WITH DRAGONFLY

The Dragonfly imaging software is a powerful commercially available platform designed for the analysis and visualization of complex imaging data. It is particularly useful in the processing and analysis of large image datasets, such as those generated from microscopy and x-ray tomography imaging. The software allows intricate image processing tasks, including segmentation, 3D reconstruction, and quantitative analysis of material structures on these large datasets. For the purposes of the previously introduced APS datasets, Dragonfly was used to identify the crack volume change of the aggregates without and with irradiation damage. A standardized approach was developed to keep that analysis as similar as possible between different samples. The datasets were imported into Dragonfly for 3D reconstruction. A median image filter with a voxel size of three (3) was used to smooth the images, which removed some of the salt and pepper noise in the image and gave a more clearly defined edge to the voids and cracks in the aggregates. Once the filter was applied, segmentation was performed to capture the cracks and voids inside the aggregates. For aggregates that were exposed to radiation, the software's ability to segment the cracks performed better for pristine aggregates with fewer cracks and voids. This result is attributed to the cracks and voids being small and more difficult to identify in the mineral phase at the resolution of the images. The segmentation was performed based on Otsu's method, which identifies an automatic intensity threshold and splits the pixels into two classes. Although the method works best on images that have a bimodal distribution, it can still be used on an image with a single peak with some manual adjustment to capture the desired areas—in this case, the crack volume. The segmentation was performed and adjusted to capture as much of the crack and void volume as possible while minimizing the capture of mineral phases that might have similar intensities. Once the segmentation was completed, a smoothing function (voxel size of 3) was used on the regions of interest (ROIs) that were segmented to remove noise from captured mineral phases and salt-and-pepper from the image. Then, the ROIs defined will show the crack in the aggregate: Figure 13 and Figure 14 show a sample slice of all aggregates after crack identification for pristine and irradiated aggregates, respectively.

Although the segmentation of the images captured a good representation of the crack volumes, it is not perfect, and some areas could be improved, as can be seen in Figure 13 and especially in Figure 14. Dragonfly supports advanced machine learning techniques that can be leveraged for image segmentation and feature extraction, and testing to identify the best methods to refine the analysis to an even greater extent is ongoing.

3.3 CRACK VOLUME RESULTS

For each aggregate scanned, a volume of voids was calculated based on the above-described image processing procedure. This was calculated as the number of pixels that were captured in the ROI captured by the segmentation. Before the segmentation was accepted, several individual slices were examined to evaluate the coverage of cracks captured by the segmentation. Table 6 shows the calculated void percentage, from Dragonfly, in the pristine and highest dose aggregates.

Table 6. Crack Volume Extracted from Dragonfly.

Irradiated		Pristine	
Aggregate	Percent voids	Aggregate	Percent voids
GB/E06	4.18%	GB/E45	0.11%
GA/F06	0.47%	GA/F45	0.08%
GC/G06	3.08%	GC/G45	0.05%
GD/H06	1.95%	GD/H45	0.08%
GE/J06	1.05%	GE/J45	0.004%
GF/K06	0.09%	GF/K45	0.01%

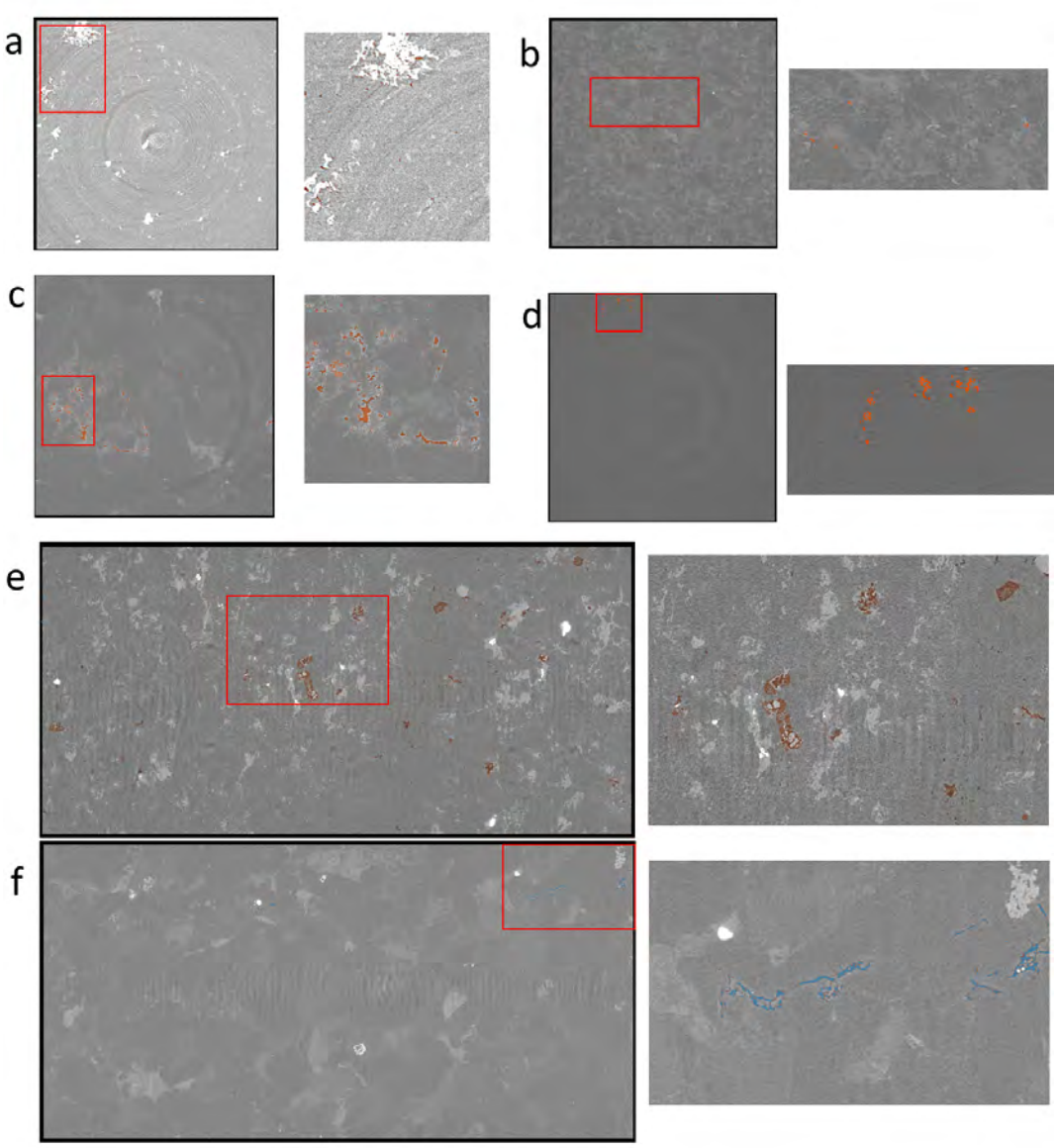

Figure 13. Dragonfly processed pristine 2D slices: a) GA/F45, b) GE/J45, c) GD/H45, d) GF/K45, e) GB/E45, f) GC/G45.

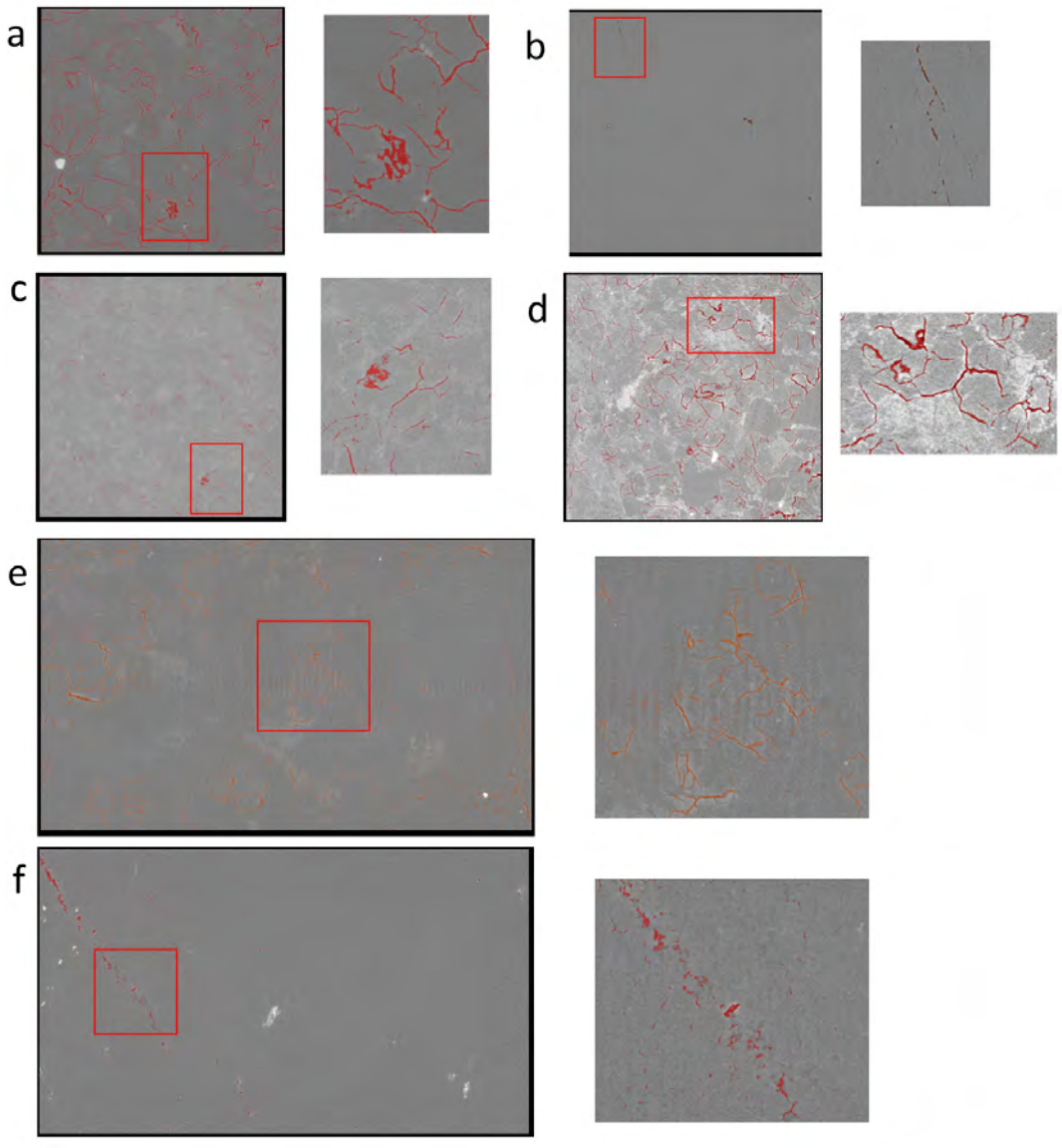

Figure 14. Dragonfly processed irradiated 2D slices: a) GB/E06, b) GF/K06, c) GE/J06, d) GC/G06, e) GD/H06, f) GA/F06.

As can be seen, all pristine aggregates have a low volume of cracks and all are increased by the irradiation dose. As expected, the amount of damage that was induced by irradiation drastically varied across the different aggregates, the highest increase being in the sandstones and the least in the limestone, then the tuff. Dragonfly produces a visual representation of the crack volume as shown in Figure 15 and Figure 16, which show the 3D reconstruction of the pristine and irradiated samples, respectively. These figures show two views of the 3D reconstruction. The first view is the crack ROI overlaid with the aggregate sample, and the second view is only the crack ROI, which is easily discernible only when the crack volume is low due to the overlapping of highlighted pixels. Although individual cracks and voids could not be distinguished as easily as crack volume goes, it still demonstrates a visual representation of the amount and dispersion of cracks through the aggregates once they are exposed to irradiation. Though it might appear that the entirety of the sample is cracked this is an illusion created by the fact that every image slice (~3000) of the sample shown by the examples in Figure 14 are stacked together. This results in a large amount of overlap when trying to view through the thickness of the sample in 3D, e.g. if slice 2900 and slice 2800 each have a crack that is only one pixel removed from the other then when viewed from the angle perpendicular to the crack in each slice it will appear that the two cracks are touching each other, when in reality they are in different areas of the sample.

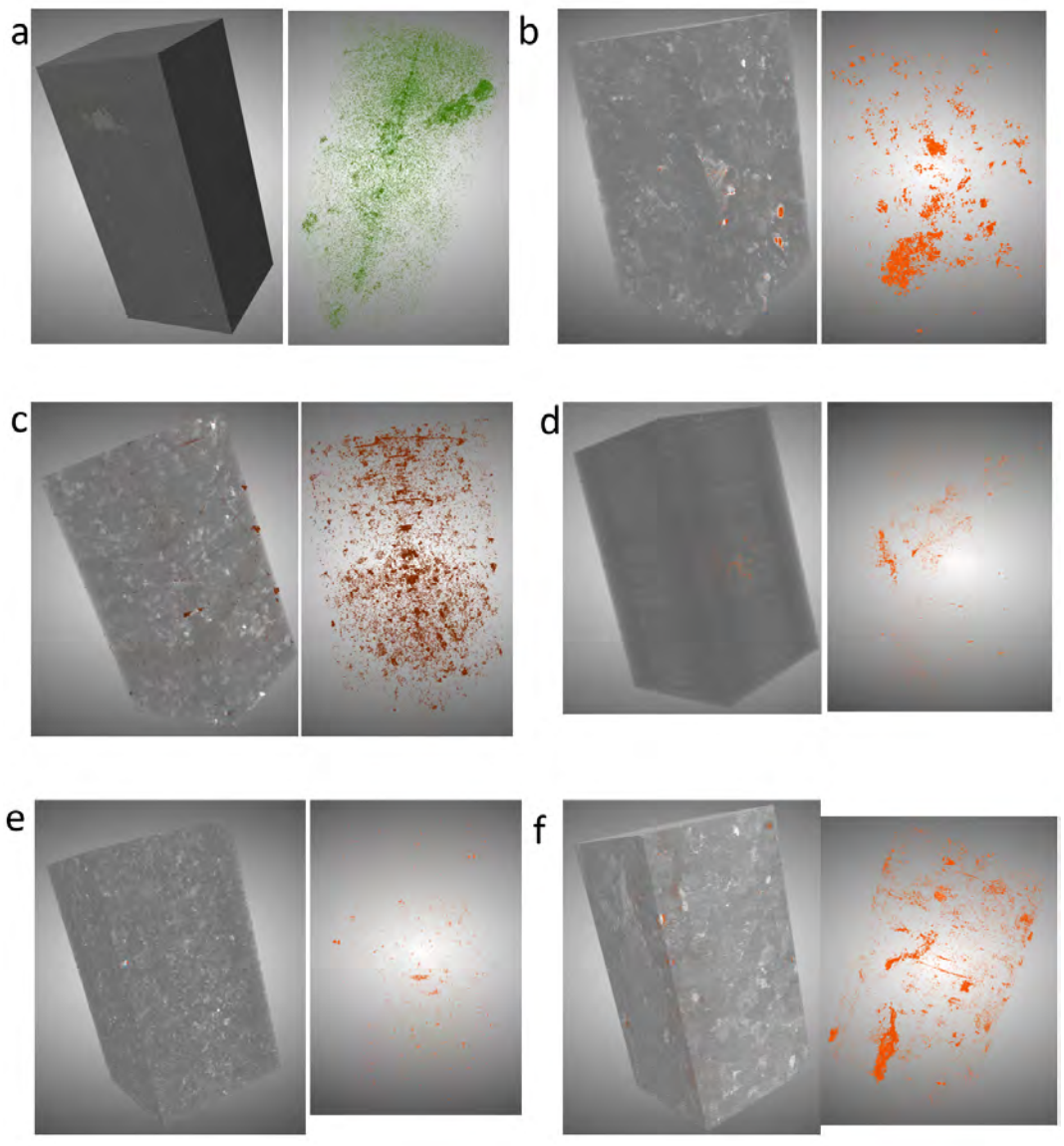

Figure 15. Dragonfly processed pristine 3D rendering: a) GA/F45, b) GD/H45, c) GB/E45, d) GF/K45, e) GE/J45, f) GC/G45.

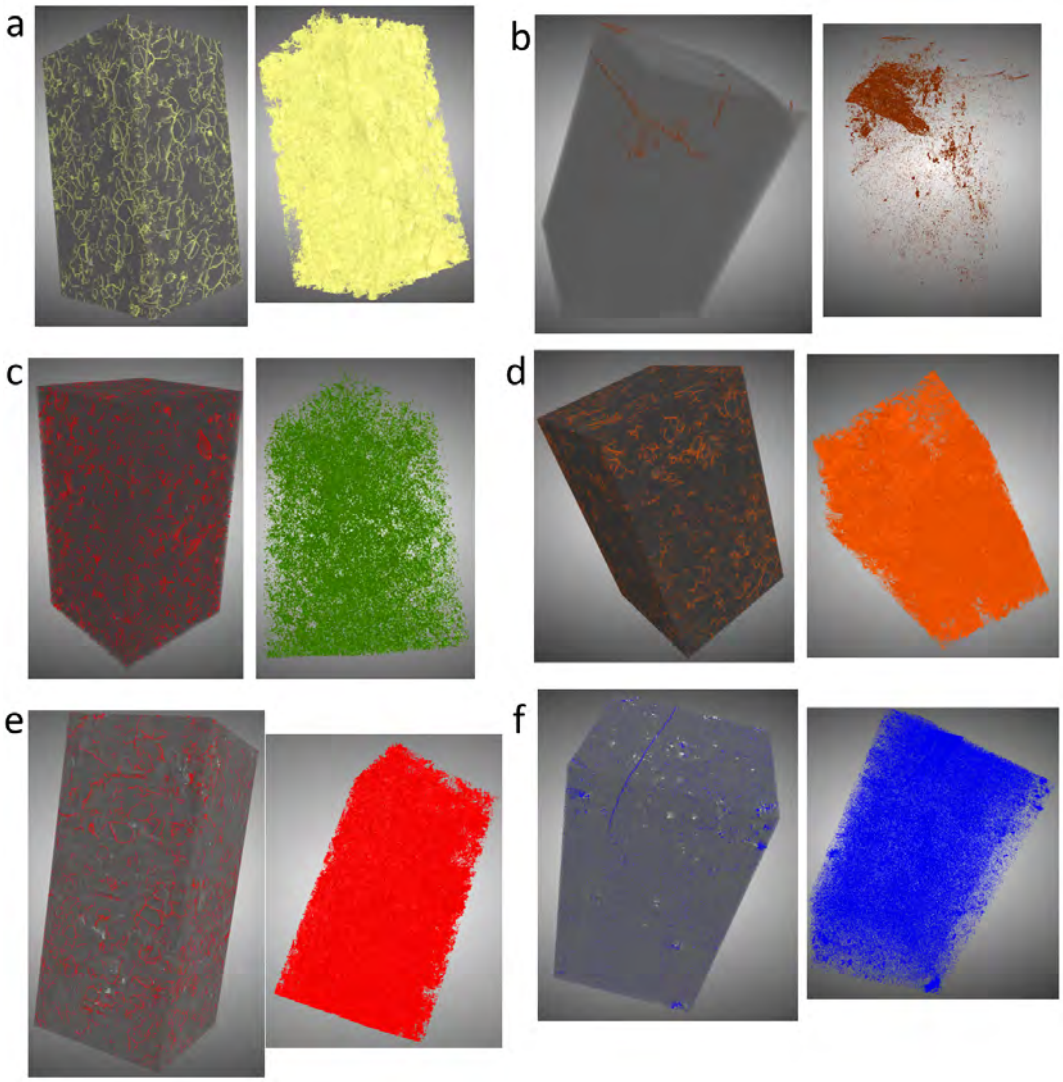

Figure 16. Dragonfly processed irradiated 3D rendering: a) GB/E06, b) GF/K06, c) GE/J06, d) GD/H06, e) GC/G06, f) GA/F06.

4. CONCLUSIONS

Neutron irradiation damage in concrete is mainly governed by aggregate RIVE. The amorphization of the crystalline structure of minerals present in aggregates after being exposed to neutrons causes their expansion, and this expansion is mineral dependent. As aggregates are rocks conformed by different minerals, a mismatch of RIVEs occurs, which gives rise to defects such as voids and cracks.

The report showcases probabilistic predictive models to estimate the irradiation damage depth in the CBS depending on aggregate mineralogy. In this study, an average composition of sedimentary rocks was used. It was concluded that the damage penetration depth is highly dependent on the aggregate volume fraction increasing with larger volume fraction. For a typical aggregate volume fraction of 0.7, the damage depth was 8 cm. The probability of damage surpassing rebar located at 3 in. from the inner surface of the CBS was 0.58 for a fluence of 0.6 n·pm^{-2} ($E > 10$ keV). This study will be repeated in the future to estimate the probability of damage penetration beyond rebar for different fluence levels.

The mechanical properties of irradiated concrete and aggregates decrease with neutron irradiation, and the accurate prediction of this decrease depends on the proper characterization of the crack volume. This report describes a method to obtain the crack volume of irradiated aggregates by image analysis of synchrotron micro-XCT scans using Dragonfly. The crack volume depends on the aggregate mineralogical origin being larger for sandstones, followed by a tuff and a limestone. This method relies on experiments that require minimal sample preparation, which offers advantages over other methods such as analysis of SEM images. This latter method is very local—probing only a small area of the sample surface, which can be misleading if a non-representative area is studied. The AI features of Dragongly will be used in the future to improve the segmentation of the cracks.

5. REFERENCES

Bykov, V.N., A.V. Denisov, V.B. Dubrovskii, V.V. Korenevskii, G.K. Krivokoneva, and L.P. Muzalevskii. 1981. "Effect of Irradiation Temperature on the Radiation Expansion of Quartz." *Atomnaya Energiya* 51 (3): 593–595.

Cheniour, A., E. Davidson, Y. Le Pape, T. Pandya, B. Collins, B. Spencer, A. Godfrey, and M. Asgari. 2023. "A structural model of the long-term degradation of the concrete biological shield." *Nuclear Engineering and Design* 405:112217. ISSN: 0029-5493. https://doi.org/https://doi.org/10.1016/j.nucengdes.2023.112217. https://www.sciencedirect.com/science/article/pii/S0029549323000663.

Denisov, A.V., V.B. Dubrovskii, and V.N. Solovyov. 2012. *Radiation Resistance of Mineral and Polymer Construction Materials.* In Russian. ZAO MEI Publishing House.

Der Kiureghian, A., and O. Ditlevsen. 2009. "Aleatory or epistemic? Does it matter?" *Structural Safety* 31 (31): 105–112. https://doi.org/10.1016/j.strusafe.2008.06.020.

Elleuch, L.F., F. Dubois, and J. Rappeneau. 1972. "Effects of Neutron Radiation on Special Concretes and Their Components." *Special Publication of The American Concrete Institute* 43:1071–1108.

Field, K.G., I. Remec, and Y. Le Pape. 2015. "Radiation Effects on Concrete for Nuclear Power Plants – Part I: Quantification of Radiation Exposure and Radiation Effects." *Nuclear Engineering and Design* 282:126–143.

Folk, R. 1980. *Petrology of Sedimentary Rocks.* 190. Hemphill Publishing Company, Austin TX.

Goldich, S.S. 1938. "A study in rock-weathering." *The Journal of Geology* 46 (1): 17–58.

Gray, B.S. 1971. "The effects of reactor radiation on cement and concrete." In *Proceedings of an Information Exchange Meeting on 'Results of Concrete Irradiation Programmes',* vol. EUR 4751 f-e. Brussels, Belgium: Commission des Communautés Européennes, April.

Hill, R. 1952. "The elastic behavior of a crystalline aggregate." *Proceedings of the Physical Society* 65:349–354.

Hilsdorf, H.K., J. Kropp, and H.J. Koch. 1978. "The Effects of Nuclear Radiation on the Mechanical Properties of Concrete." *Special Publication of The American Concrete Institute* 55:223–254.

Hsiao, Y.-H., E. Callagon La Plante, N.M.A. Krishnan, H.A. Dobbs, Y. Le Pape, N. Neithalath, M. Bauchy, J. Israelachvili, and G. Sant. 2018. "Role of the electrical surface potential and irradiation induced disordering on almandine's dissolution kinetics." Submitted, *The Journal of Physical Chemistry C* 122 (30): 17268–17277.

Hsiao, Y.-H., E. La Plante, N.M.A. Krishnan, Y. Le Pape, N. Neithalath, M. Bauchy, and G. Sant. 2017. "Effects of Irradiation on Albite's Chemical Durability." Submitted, *The Journal of Physical Chemistry A* 121:7835–7845.

Hsiao, Y.-H., B. Wang, E. Callagon La Plante, I. Pignatelli, N.M.A. Krishnan, Y. Le Pape, N. Neithalath, M. Bauchy, and G. Sant. 2019. "The effect of irradiation on the atomic structure and chemical durability of calcite and dolomite." Accepted, *npj Materials Degradation,* https://doi.org/10.1038/s41529-019-0098-x.

Kambayashi, D., S. Sasano H. Sawada, K. Suzuki, and I. Maruyama. 2020. "Numerical Analysis of a Concrete Biological Shielding Wall under Neutron Irradiation by 3D RBSM." *Journal of Advanced Concrete Technology* 18:617–632.

Keller, W.D. 1954. "The bonding energies of some silicate minerals." *American Mineralogist* 39:783–793.

Khmurovska, Y., P. Štemberk, T. Fekete, and T. Eurajoki. 2019. "Numerical analysis of VVER-440/213 concrete biological shield undernormal operation." *Nuclear Engineering and Design* 350:58–66.

Krishnan, A.N.P., Y. Le Pape, G. Sant, and M. Bauchy. 2018. "Effect of irradiation on silicate aggregates' density and stiffness." *Journal of Nuclear Materials* 512 (October 8, 2018): 126–136. https://doi.org/10.1016/j.nucmat.2018.10.009.

———. 2019. "Disorder-Induced Expansion of Silicate Minerals Arises from the Breakage of Weak Topological Constraints." Submitted, *Physical Review Letters.*

Krivokoneva, G.K. 1976. "Structural Changes in feldspars under Impact of Radiation." (In Russian), *Crystal Chemistry and Structural Features of Minerals* Leningrad, Nauka:75–79.

Krivokoneva, G.K., and G.A. Sidorenko. 1971. "The essence of the metamict transformation in pyrochlores." *Geochemistry International* 8:113–122.

Kupfer, H., H.K. Hilsdorf, and H. Rüsch. 1969. "Behavior of concrete under biaxial stresses." *Journal of the American Concrete Institute* 66:656–666.

Le Pape, Y. 2015. "Structural Effects of Radiation-Induced Volumetric Expansion on Unreinforced Concrete Biological Shields." *Nuclear Engineering and Design* 295:534–548.

Le Pape, Y., M.H.F. Alsaid, and A.B. Giorla. 2018. "Rock-forming minerals radiation-induced volumetric expansion – Revisiting the literature data." *Journal of Advanced Concrete Technology* 16:191–209. https://doi.org/10.3151/jact.16.191.

Le Pape, Y., K.G. Field, and I. Remec. 2015. "Radiation Effects in Concrete for Nuclear Power Plants – Part II: Perspective from Micromechanical Modeling." *Nuclear Engineering and Design* 282:144–157.

Le Pape, Y., S. Sabatino, and Tajuelo Rodriguez. 2023. *Effects of Aggregates Mineralogy on the Irradiation-Induced Damage in Concrete Biological Shields.* Technical report ORNL/SPR-2023/2912. Oak Ridge National Laboratory.

Le Pape, Y., J. Sanahuja, and M.H.F. Alsaid. 2020. "Irradiation-Induced Damage in Concrete-Forming Aggregates – Revisiting Literature Data Through Micromechanics." *Materials and Structures* 53 (62): 35. https://doi.org/10.1617/s11527-020-014.

Levenberg, K. 1944. "A Method for the Solution of Certain Non-Linear Problems in Least Squares." *Quarterly of Applied Mathematics* 2:164–168.

Marquardt, D. 1963. "An Algorithm for Least-Squares Estimation of Nonlinear Parameters." *SIAM Journal on Applied Mathematics* 11 (2): 431–441.

Maruyama, I., K. Haba, O. Sato, S. Ishikawa, O. Kontani, and M. Takizawa. 2016. "A numerical model for concrete strength change under neutron and gamma-ray irradiation." *Journal of Advanced Concrete Technology* 14:144–162.

Maruyama, I., T. Kondo, S. Sawada, P. Halodova, A. Fedorikova, T. Ohkubo, K. Murakami, T. Igari, E. Tajuelo Rodriguez, and K. Suzuki. 2022. "Radiation-induced Alteration of Meta-chert." *Journal of Advanced Concrete Technology* 20 (12): 760–776. https://doi.org/10.3151/jact.20.760.

Maruyama, I., T. Kondo, S. Sawada, P. Halodova, A. Fedorikova, T. Okhubo, K. Murakami, et al. 2023. "Radiation-induced alteration of sandstone concrete aggregate." *Journal of Nuclear Materials* 583:154547. https://doi.org/10.1016/j.jnucmat.2023.154547.

Maruyama, I., O. Kontani, M. Takizawa, S. Sawada, S. Ishikawa, J. Yasukouchi, O. Sato, J. Etoh, and T. Igari. 2017. "Development of the Soundness Assessment Procedure for Concrete Members Affected by Neutron and Gamma-Irradiation." *Journal of Advanced Concrete Technology* 15:440–523.

Maruyama, I., A. Teramoto, and G. Irashi. 2014. "Strain and thermal expansion coefficients of various cementpastes during hydration at early ages." *Materials and Structures* 47:27–37.

Mayer, G, and M Lecomte. 1960. "Effet des neutrons rapides sur le quartz cristallin et la silice vitreuse." *Le Journal de Physique et le Radium* 21 (12): 846–852.

Mayer, G., and J. Gigon. 1956. "Effets des neutrons rapides sur quelques constantes physiques du quartz cristallin et de la silice vitreuse." *Le Journal de Physique et le Radium* 18:109–114.

Mazars, J., and G. Pijaudier-Cabot. 1989. "Continuum Damage Theory –Application to Concrete." *Journal of Engineering Mechanics – ASCE* 115:345–365.

Perkins, D. 2022. "Mineralogy, Chapter 7: 7 Sedimentary Minerals and Sedimentary Rocks." Accessed August 26, 2024. https://opengeology.org/Mineralogy/7-sedimentary-minerals-and-sedimentary-rocks/.

Pignatelli, I., A. Kumar, K.G. Field, B. Wang, Y. Yu, Y. Le Pape, M. Bauchy, and G. Sant. 2016. "Direct Experimental Evidence for Differing Reactivity Alterations of Minerals following Irradiation: The Case of Calcite and Quartz." Accepted for publication, *Scientific Reports – Nature* 6(20155):1–10. https://doi.org/10.1038/srep20155.

Pomaro, B., V.A. Salomoni, F. Gramegna, G. Prete, and C.E. Majorana. 2011. "Radiation damage evaluation on concrete within a facility for Selective Production of Exotic Species (SPES Project), Italy." *Journal of Hazardous Materials* 194 (0): 169–177. ISSN: 0304-3894.

Primak, W. 1958. "Fast-Neutron-Induced Changes in Quartz and Vitreous Silica" [in English]. *Physical Review* (One Physics Ellipse, College PK, MD 20740-3844 USA) 110 (6): 1240–1254. ISSN: 0031-899X.

———. 1976. "Extrusion of quartz on ion bombardment: Further evidence for radiation-induced stress relaxation of the silica network" [in English]. *Physical Review B* (One Physics Ellipse, College Pk, MD 20740-3844 USA) 14 (10): 4679–4686. ISSN: 0163-1829.

Primak, W., and R. Kampwirth. 1968. "The radiation compaction of vitreous silica." *Journal of Applied Physics* 39 (12): 5651–5658.

Rankine, W. 1857. "On the stability of loose earth." *Philosophical Transactions of the Royal Society of London* 147:9–27.

Remec, I., T.M. Rosseel, K.G. Field, and Y. Le Pape. 2014. "Characterization of Radiation Fields in Biological Shields of NPPs for Assessing Concrete Degradation." In *Proceedings of the Fifteenth International Symposium on Reactor Dosimetry.* Aix-en-Provence, France, May.

Reuss, A. 1929. "Berechnung der Fließgrenz von Mischkristallen auf Grund der Plasticitätsbedingung für Einkristalle." *Zeitschrift für Angewandte Mathematik und Mechanik* 9:49–58.

Seeberger, J., and H.K. Hilsdorf. 1982. *Einfluss von radioactiver Strahlung auf die Festogkeit and Struktur von Beton.* Technical report NR 2505. Institut fur Massivbau and Baustofftechnologie, Universitat Karlsruhe.

Sellevold, E.J., and O. Bjontegaard. 2006. “Coefficient of thermal expansion of cement paste andconcrete: Mechanisms of moisture interaction.” 39:809–815.

Tajuelo Rodriguez, E., D. Arregui-Mena, A. Cheniour, Y. Li, Y. Le Pape, L. M. Anovitz, M. C. Cheshire, et al. 2021. *Multi-Technique Characterization of Porosity and Cracks in Pristine and Neutron-Irradiated Aggregates Complemented by Mosaic Simulations.* Technical report ORNL/TM-2024/3287. Oak Ridge National Laboratory.

Voigt, W. 1889. “Über die Beziehung zwischen den beiden Elasticitätskonstanten isotroper Körper.” *Annalen der Physik* 274:573–587.

Wang, B., A. Krishnan, Y. Yu, M. Wang, Y. Le Pape, G. Sant, and M. Bauchy. 2017. “Irradiation-Induced Topological Transition: Structural Signature of Networks’ Rigidity.” Accepted, *Journal of Non-Crystalline Solids* 463:25–30.

Whitney, D.L., and B.W. Evans. 2010. “Abbreviations for names of rock-forming minerals.” *American Mineralogist* 95:185–187.

Wilson, M.J. 2004. “Weathering of the primary rock-forming minerals: processes, products and rates.” *Clay Minerals* 39:233–266.

Wong, C.F. 1974. “Neutron radiation damage in some birefringent crystals.” *Physics Letters A* 50 (5): 346.

Zubov, V.G., and A.T. Ivanov. 1966. “Expansion of quartz caused by irradiation with fast neutrons.” *Soviet Physics Crystallography* 11 (3): 372–374.